PNC TN8410 96-058

COUPLED THERMO - HYDRO - MECHANICAL
EXPERIMENT AT KAMAISHI MINE

TECHNICAL NOTE 07-95-07

HYDRAULIC TESTS

M. Chijimatsu, T. Fujita, Y. Sugita and H. Ishikawa
Power Reactor and Nuclear Fuel Development Corporation (PNC)

A. Kobayashi
Iwate University

公　開　資　料
PNC TN8410 96-058
１９９６年２月

釜石原位置試験場における粘土充填・熱負荷試験
テクニカルノート　07-95-07
透水試験結果

千々松正和*1・藤田朝雄*1・杉田裕*1・石川博久*1・小林晃*2

要　旨

地層処分における技術開発の観点からは、工学規模での試験によるニアフィールド環境である周辺岩盤の挙動が人工バリアに与える影響の把握および周辺岩盤を含むニアフィールド性能の定量的評価と室内および原位置における大型試験による人工バリアの品質性能の確認を行い、地層処分技術の信頼性向上を図ることが重要となっている。そのため、動力炉・核燃料開発事業団東海事業所の地層処分基盤研究施設等における工学規模の試験と並行して、原位置試験場において、人工バリアの品質性能の確認およびその実岩盤条件下でのニアフィールド連成挙動を評価することが必要となっている。

そこで、実条件でのニアフィールド環境を把握するため釜石原位置試験場において粘土充填・熱負荷試験を実施している。

本論では、試験領域内の水理特性を把握するために実施した透水試験の結果を報告する。透水試験には７本の試錐孔を使用した。その内の３本には間隙水圧計システムを設置し、観測用とした。残りの試錐孔を使用し、定圧力注入透水試験と定流量透水試験の２種類の試験を実施した。試験の結果、試験領域の透水性は全体的に低く、その中に存在する透水性亀裂が水みちとなっていることが分かった。また、試験結果を用い、透水係数の次元解析及び透水テンソルの算定を行なった。

---

*1 東海事業所　環境技術開発部　地層処分開発室

*2 岩手大学　農学部

PNC TN8410 96-058
February, 1996

COUPLED THERMO-HYDRO-MECHANICAL EXPERIMENT AT KAMAISHI MINE

TECHNICAL NOTE 07-95-07

HYDRAULIC TESTS

ABSTRACT

It is an important part of the near field performance assessment of nuclear waste disposal to evaluate coupled thermo-hydro-mechanical (T-H-M) phenomena, e.g., thermal effects on groundwater flow through rock matrix and water seepage into the buffer material, and generation of the swelling pressure of the buffer material, and thermal stresses potentially affecting porosity and fracture aperture of the rock. An in-situ T-H-M experiment, which is named 'Engineered Barrier Experiment', has been conducted at the Kamaishi Mine, of which host rock is granodiorite, in order to establish conceptual models of coupled T-H-M processes and to build confidence to the mathematical models and computer codes.

This note describes the results of hydraulic tests. After fracture survey, hydraulic tests were conducted in a cluster of seven boreholes to obtain the hydraulic properties at the Kamaishi T-H-M experiment site. Using seven boreholes, two type tests were conducted, one was injection test at a constant pressure, and the other was at a constant flow rate. As a result of tests, it is conceivable that the permeability at this site is small as a whole but small number of high permeable fractures exist. Then dimensional analysis was applied to the results and distribution of dimensional hydraulic properties were examined, which will help to consider the statistical characteristics of the site.

COUPLED THERMO-HYDRO-MECHANICAL EXPERIMENT AT KAMAISHI MINE

TECHNICAL NOTE 07-95-07

HYDRAULIC TESTS

CONTENTS

1. INTRODUCTION

Power reactor and Nuclear Fuel Development Corporation (PNC) has conducted the activities of geoscientific R&D program. In order to understand the deep geological condition in fractured crystalline rock, PNC initiated the in-situ experiments in the Kamaishi Mine, where early Cretaceous granodiorite hosts the experiments [1,2].

The coupled thermo-hydro-mechanical (T-H-M) experiment in situ has been planned as a task of Kamaishi in-situ experiments in order to establish the coupled T-H-M conceptual models and to build up confidence to the mathematical models and computer codes. The program of T-H-M experiment is divided into five phases; Excavation of Drifts, Measurement of Rock Properties, Excavation of Test Pit, Setting up of Bentonite, and T-H-M test [3]. The experimental drift was opened, 5m×10m in square and 7m in height, by drill and blast method and then seven boreholes were drilled. At first we carried out fracture surveys and reported about statistical characterization of fracture geometry [4].

After fracture survey, hydraulic tests were conducted in a cluster of seven boreholes to obtain the hydraulic properties at the Kamaishi T-H-M experiment site. This report describes the results of hydraulic tests.

2. LAYOUT OF EXPERIMENT

The Kamaishi Mine is located approximately 600km north of Tokyo. The bedrock in this area consists of Paleazoic sedimentary rock, Cretaceous sedimentary rock and igneous complexes. The facilities of T-H-M experiment are located at a drift 550m above sea level (EL 550m drift) in the Cretaceous-age Kurihashi granodiorite. The statistical characterization of fracture geometry of the test site are described by Fujita et al. [4].

Figure 1 shows the location of seven boreholes at the test site. This figure also shows the fracture map on the floor of the experimental drift. Borehole KBH7 is the center of the test pit. Orientation, length, diameter and coordinate data for the boreholes are given in Table 1.

Table 1 Orientation, length and diameter data

Borehole	Dip direction	Dip	Length	Diameter	Coordinate(m)		
	(deg)	(deg)	(m)	(mm)	X	Y	Z
KBH1	-	90	8.0	66	-10.338	-11.764	-2.373
KBH2	-	90	8.0	66	-10.301	-12.237	-2.267
KBH3	349	79	8.0	66	-9.189	-10.534	-2.519
KBH4	347	79	8.0	66	-8.611	-10.509	-2.499
KBH5	-	90	8.0	66	-11.603	-9.306	-2.283
KBH6	-	90	8.0	66	-12.035	-8.896	-2.282
KBH7		90	8.0	76	-10.571	-10.356	-2.357

3. HYDRAULIC TEST

3.1 TEST 1

After excavation of the boreholes, water level in each borehole was measured. Figure 2 shows the results. Although all boreholes were excavated near each other, water levels were quite different. Prior to the hydraulic test, packers and piezometers were set up in the monitoring holes KBH1, KBH3 and KBH5. Figure 3 shows the location of packers in boreholes KBH1, KBH3 and KBH5. Five intervals in each hole were isolated using pneumatic packers. Each interval was equipped with piezometer. Figure 3 also shows fracture location in boreholes, in which strike and dip are not taken into consideration. Straight lines are open fractures and dotted lines are closed fractures. Taking these fracture locations into account, locations of packers were decided.

Injection was carried out at other boreholes (KBH2, KBH4, KBH6, KBH7). Boreholes KBH2, KBH4 and KBH6 had seven injection intervals and borehole KBH7 had six injection intervals, each 1m, as shown in Figure 3. Figure 4 shows the initial pressure distributions in the injection holes. Pressures of borehole KBH7 were quite high compared to other boreholes. Using these boreholes two type tests were conducted, one was injection test at a constant pressure, and the other was at a constant flow rate. Constant pressure tests were conducted using all injection intervals. In these tests injection flow rates over $1cm^3/min$ were measured. Then constant injection flow rate tests were carried out at a few intervals, where injection flow rate at the time of constant pressure tests were relatively higher.

Figures 5-8 show the time history of injection pressure and injection flow rate at the constant pressure tests. In the borehole KBH2, flow rates of three sections were over $1cm^3/min$. In the same way, at three sections of borehole KBH4, three sections of borehole KBH6 and five sections of borehole KBH7, flow rate were over $1cm^3/min$. Table 2 shows the results of constant pressure tests. Prior to injection, initial pressure heads were measured at injection intervals. From this result, it is known that initial pressure head does not show hydrostatic pressure distribution and borehole KBH7 crosses high pressure zone. Each borehole has one injection interval where injection flow rate is much higher than other intervals of the same borehole. When injection was carried out at these sections, a few responses at monitoring sections in monitoring boreholes were observed. Observed response sections are also given in Table 2. There are open fractures at these injection intervals and response sections. It indicates that these fractures are permeable. In this table, the injection flow rates at the sections where constant flow rate tests were carried out were given. Figures 9-12 show the time history of injection pressure and injection flow rate at the constant flow rate tests. In the case of constant injection test, increase of injection pressure

was slow. Furthermore it reveals that it took more time to be steady state as the section's permeability decreased.

3.2 HYDRAULIC CONDUCTIVITY

Using the results of constant pressure test, permeability at the injection sections were obtained from eq.(1)

$$k = \frac{Q}{2\pi L h} ln(\frac{L}{r_w}) \qquad (1)$$

where k(cm/s) is the permeability, Q(cm^3/s) is the injection flow rate, L(cm) is the injection interval length, h(cm) is the pressure head, r_w(cm) is the radius of boreholes.

Figure 13 shows the permeability distributions in the injection boreholes. Permeability at the section where injection flow rate is lowered than 1.0cm^3/min is smaller than 10^{-8}cm/s. This figure predicts there is high permeable zone at the approximately 3m depth. Figure 14 shows the result of observed connections. There were few connections, and connections were only observed when injections were carried out at the high permeable sections. However, connections between the high permeable sections and the zone at the approximately 3m depth were few. Therefore, it is conceivable that high permeable zone does not exist and all injection boreholes cross the permeable fractures accidentally at the approximately 3m depth. These results reveal that the permeability at this site is small as a whole but a small number of high permeable fractures exist.

3.3 TEST 2

After TEST 1, packers and piezometers were set up in the boreholes KBH2, KBH4 and KBH6. The results of TEST 1 indicated that open fracture at the approximately 2m depth in borehole KBH3

was permeable. Then packers and piezometers in the borehole KBH3 were pushed off by 20cm aloft. About borehole KBH7, the section from 2m to 4m depth showed high permeability, so injected interval was set up at this section. Figure 15 shows the locations of injected/monitoring sections in boreholes KBH1 - 7. In this condition, initial pressures were measured again. Figure 16 shows the results. Constant pressure injection was carried out at each injected section and responses were monitored at the other sections to obtain connectivity. Figure 17 shows the result. Injection tubes installed at the sections of boreholes KBH1 - 6 are very thin, so it was very difficult to inject satisfactorily to the high permeable sections. For this reason, responses were not observed at the all sections even if injection was carried out at the high permeable section.

Table 2 Results of constant pressure test

KBH2		ϕ	66 mm				
Depth G.L.(m)	Section	Length (m)	Initial Pressure (kgf/cm^2)	Injection Pressure (kgf/cm^2)	Flow Rate (cm^3/min)	Response section	Injection test at constant flow rate (cm^3/min)
1～2	KBH2;1	1	0.05	3	9.0		10
2～3	KBH2;2	1	0.06	3	<1		
3～4	KBH2;3	1	0.07	3	3300.0	KBH1-1	3000
4～5	KBH2;4	1	0.14	3	<1		
5～6	KBH2;5	1	0.37	3	<1		
6～7	KBH2;6	1	0.3	3	<1		
7～8	KBH2;7	1	0.05	3	7.9		8

KBH4		ϕ	66 mm				
Depth G.L.(m)	Section	Length (m)	Initial Pressure (kgf/cm^2)	Injection Pressure (kgf/cm^2)	Flow Rate (cm^3/min)	Response section	Injection test at constant flow rate (cm^3/min)
1～2	KBH4;1	1	0	3	<1		
2～3	KBH4;2	1	0	3	700.0	KBH1-4,5-5	700
3～4	KBH4;3	1	0.15	3	<1		
4～5	KBH4;4	1	0.14	3	6.1		6
5～6	KBH4;5	1	0.29	3	3.7		
6～7	KBH4;6	1	0.48	3	<1		
7～8	KBH4;7	1	0.79	3	<1		

KBH6		ϕ	66 mm				
Depth G.L.(m)	Section	Length (m)	Initial Pressure (kgf/cm^2)	Injection Pressure (kgf/cm^2)	Flow Rate (cm^3/min)	Response section	Injection test at constant flow rate (cm^3/min)
1～2	KBH6;1	1	0	3	2.5		
2～3	KBH6;2	1	0.14	3	2.7		5
3～4	KBH6;3	1	0.14	3	2600.0	KBH5-1	2500
4～5	KBH6;4	1	0.5	3	<1		
5～6	KBH6;5	1	0.66	3	<1		
6～7	KBH6;6	1	0.59	3	<1		
7～8	KBH6;7	1	0.55	3	<1		

KBH7		ϕ	76 mm				
Depth G.L.(m)	Section	Length (m)	Initial Pressure (kgf/cm^2)	Injection Pressure (kgf/cm^2)	Flow Rate (cm^3/min)	Response section	Injection test at constant flow rate (cm^3/min)
2～3	KBH7;1	1	1.1	4	94.1		120
3～4	KBH7;2	1	0.07	3	1470.0	KBH1-3,4,5	1500
4～5	KBH7;3	1	4.1	5	1.6		
5～6	KBH7;4	1	3.3	4	1.8		
6～7	KBH7;5	1	1.5	3	19.0		18
7～8	KBH7;6	1	0.6	3	<1		

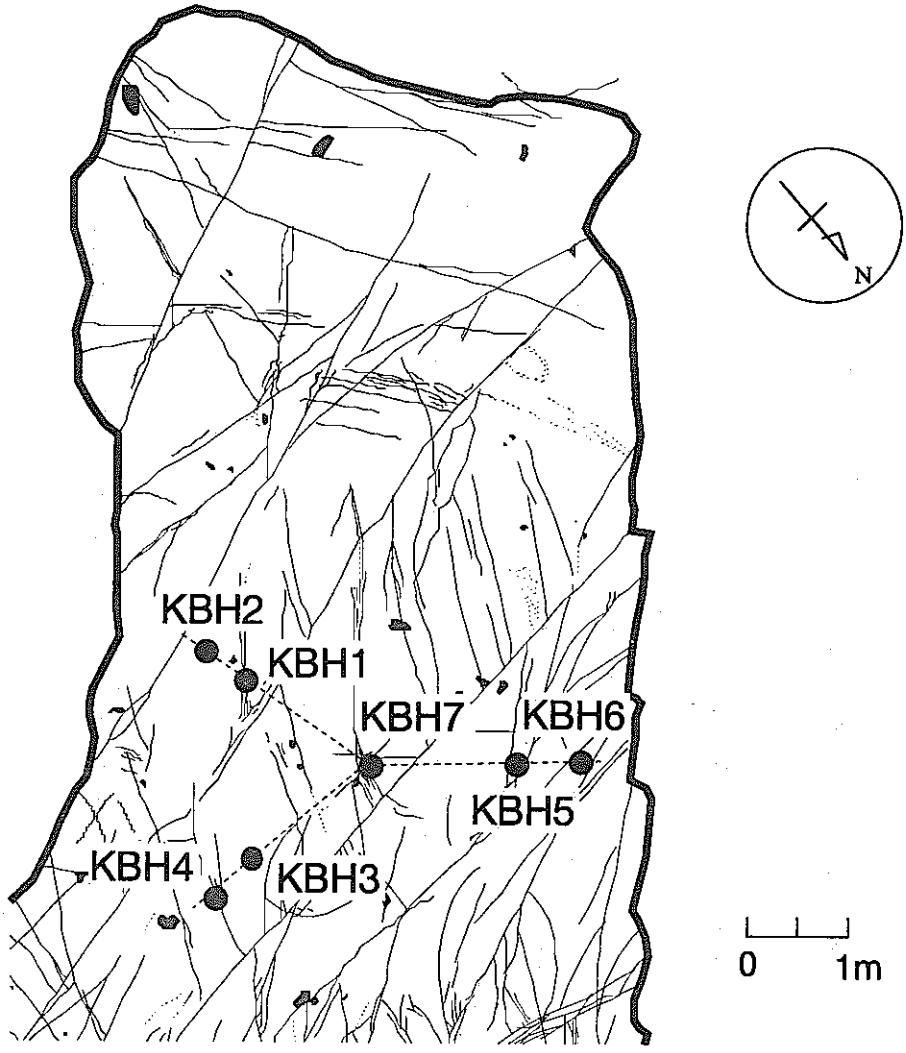

Figure 1 Location of boreholes

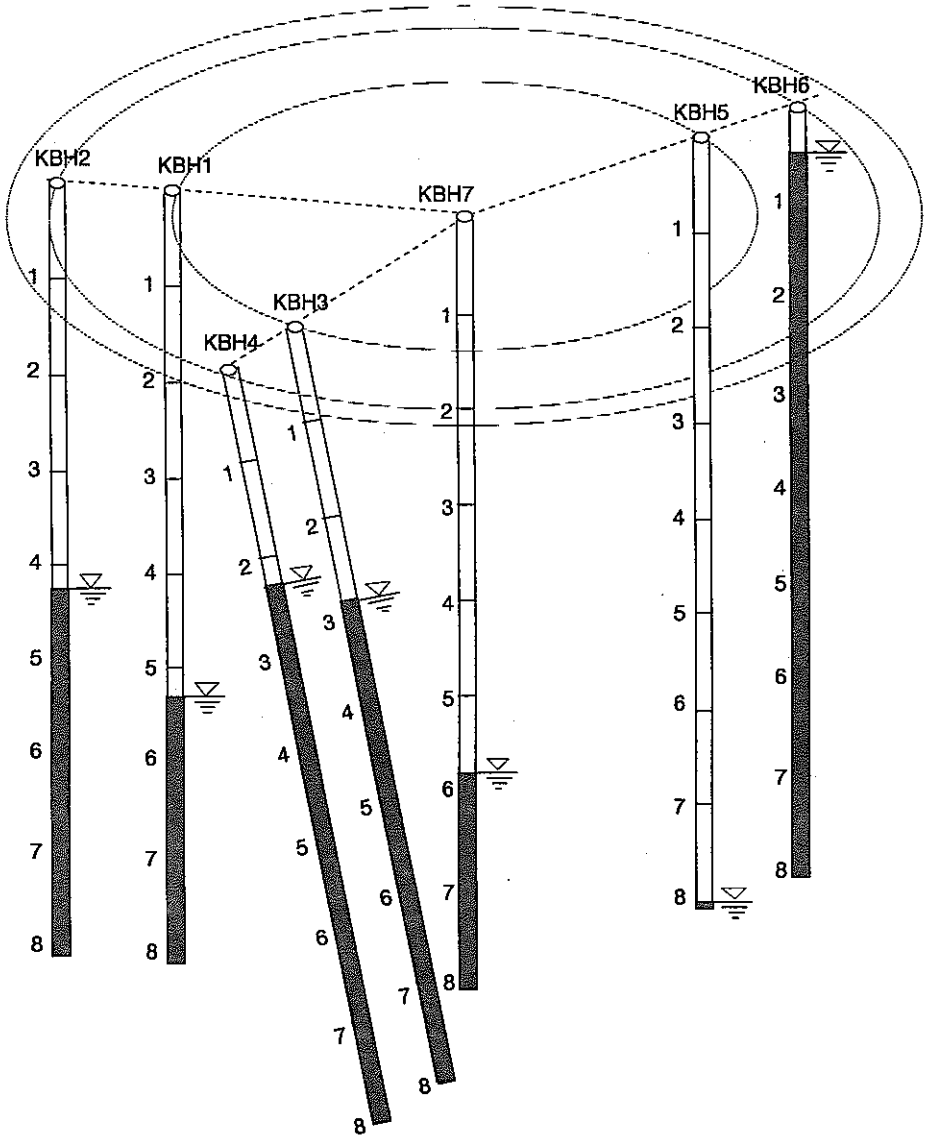

Figure 2 Water levels in the boreholes.

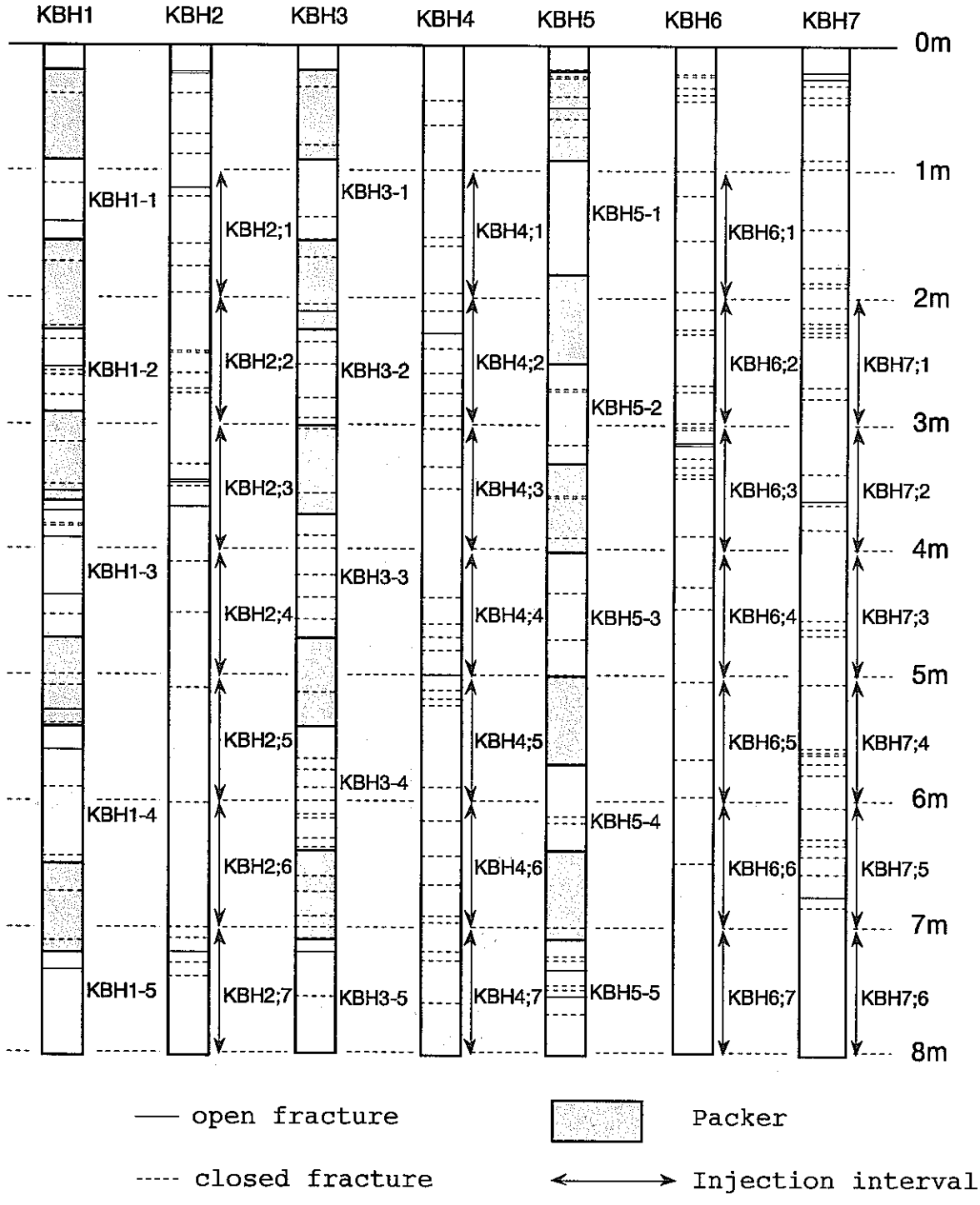

Figure 3 Location of packers and fractures in the boreholes

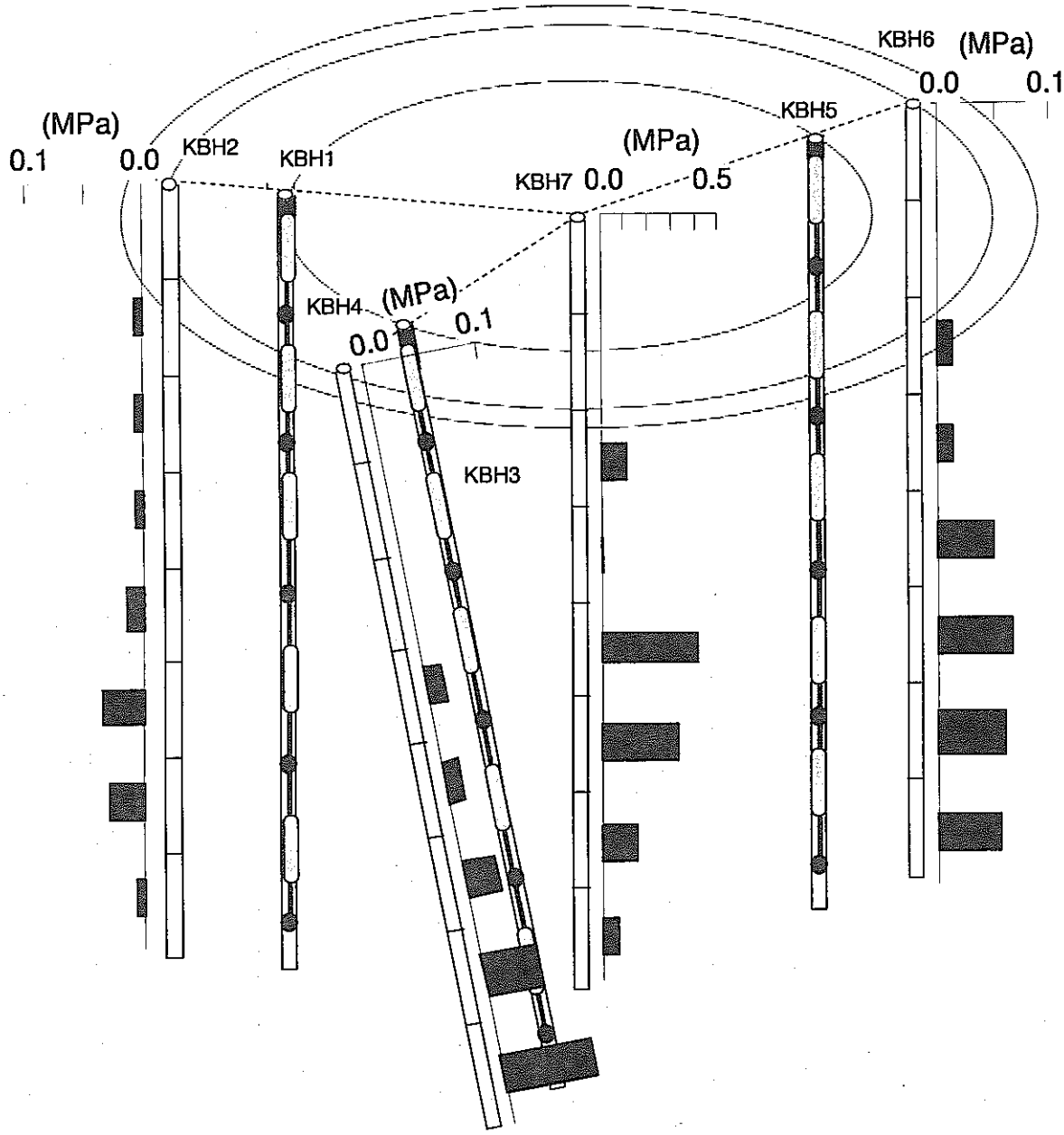

Figure 4 Initial pressure distribution before TEST 1.

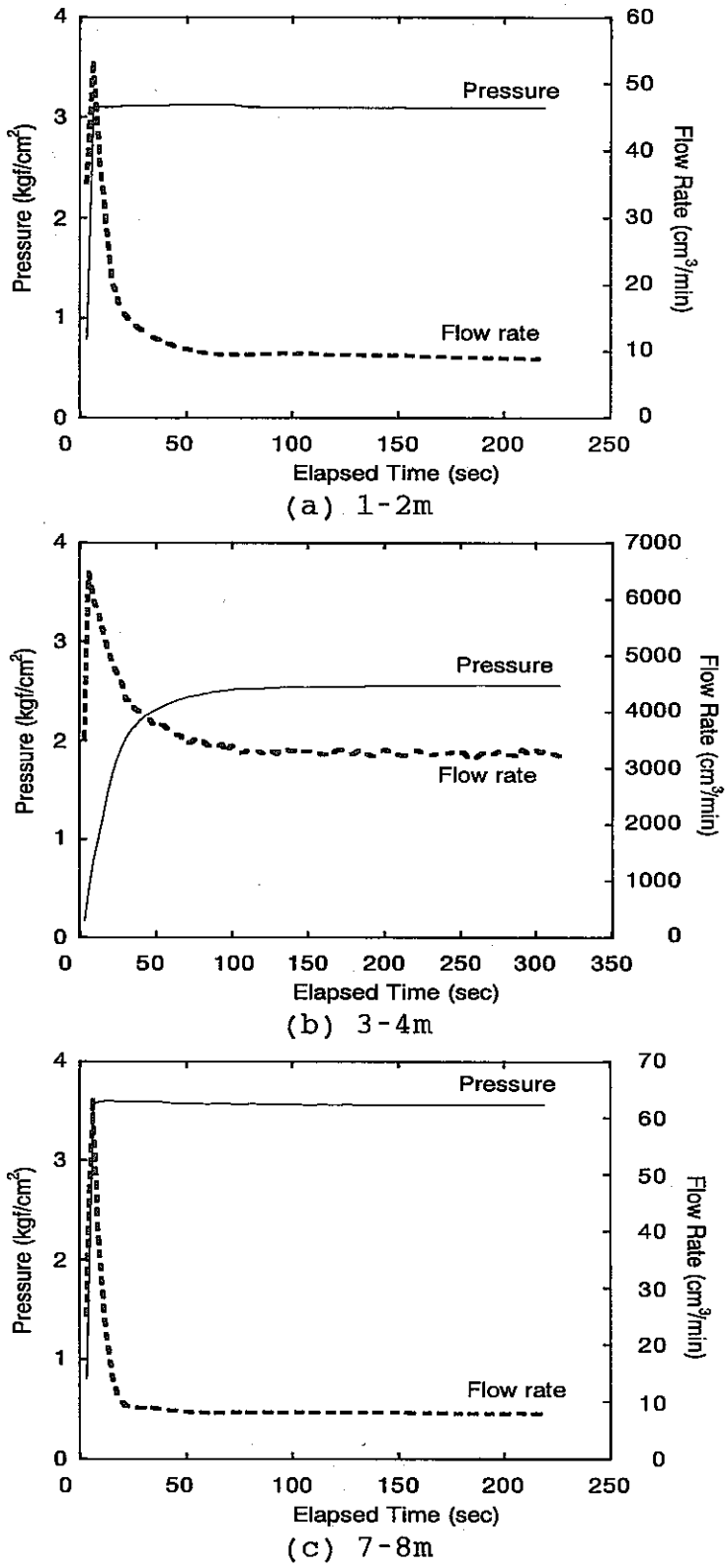

Figure 5 Time history of pressure and flow rate at the injection section(KBH2) Injection test at a constant pressure head

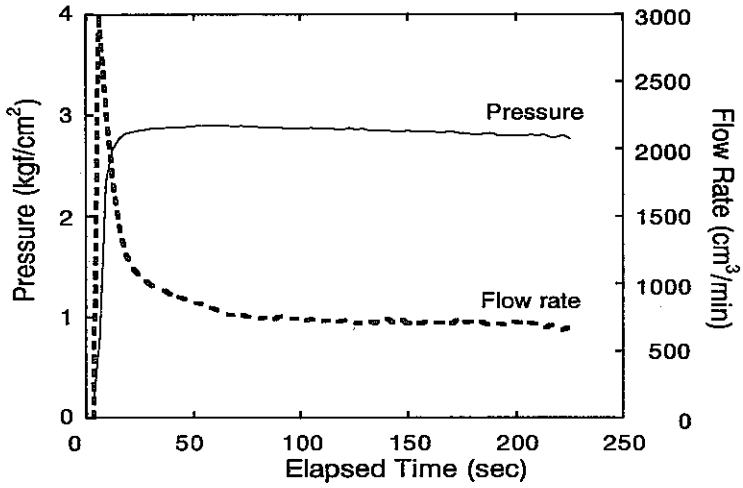

(a) 2-3m

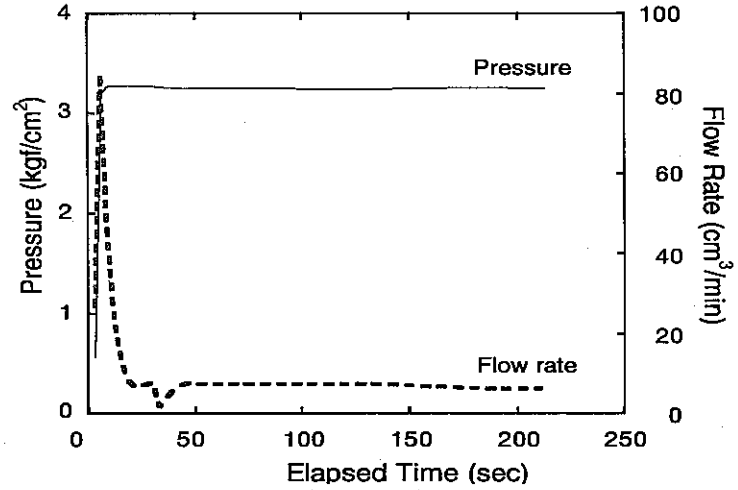

(b) 4-5m

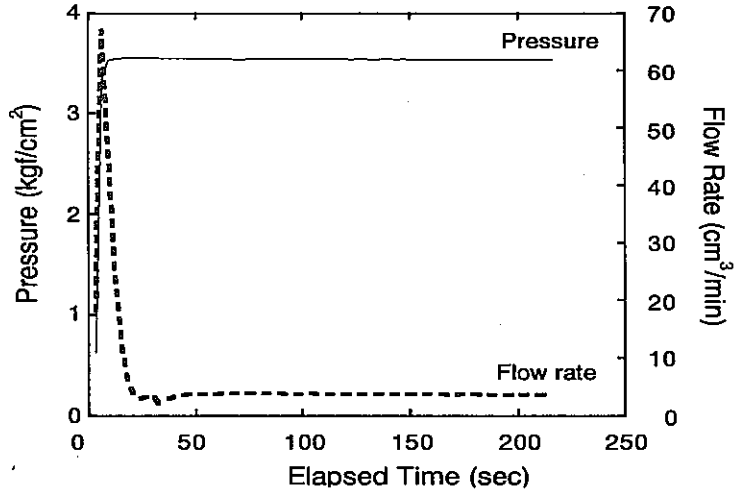

(c) 5-6m

Figure 6 Time history of pressure and flow rate at the injection section(KBH4) Injection test at a constant pressure head

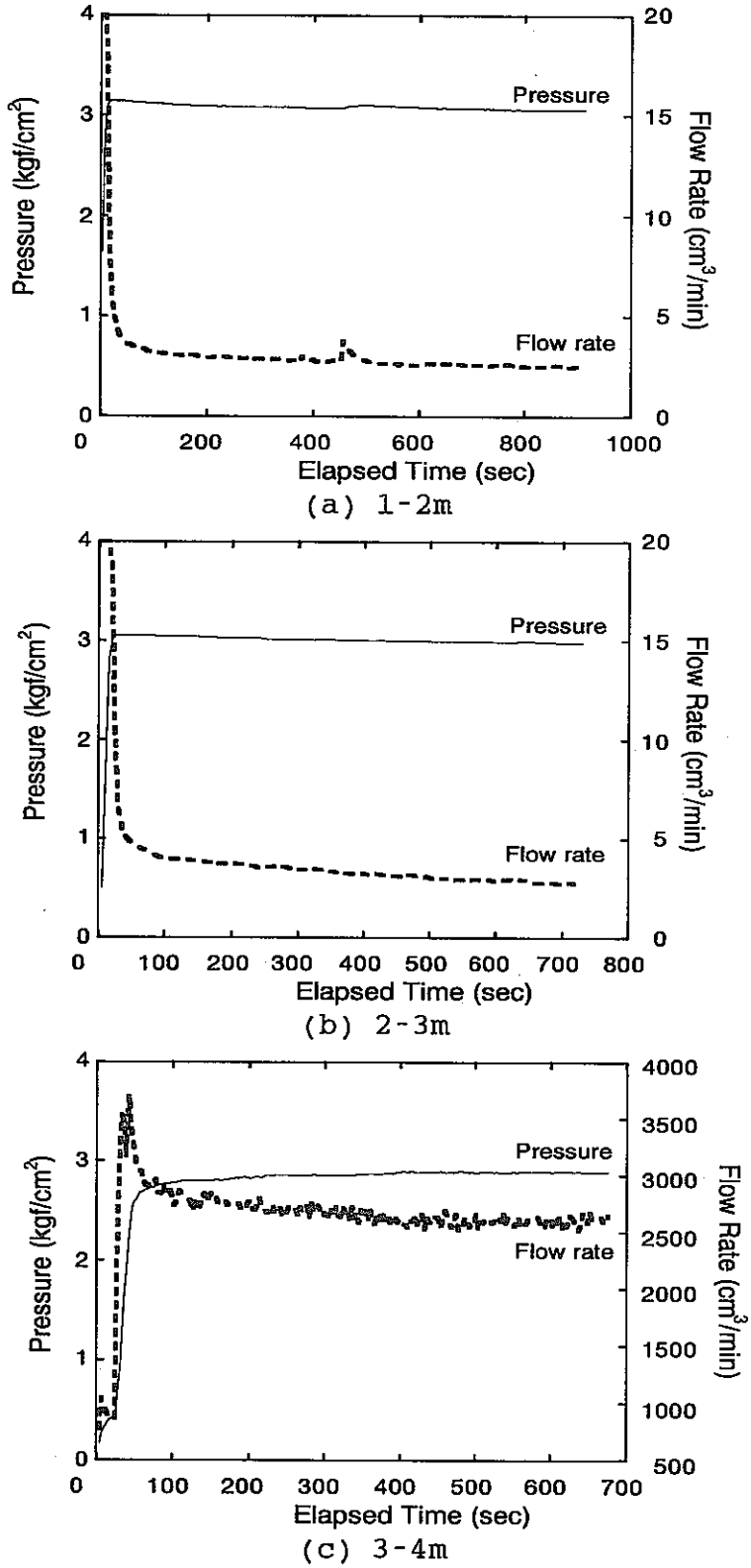

Figure 7 Time history of pressure and flow rate at the injection section(KBH6) Injection test at a constant pressure head

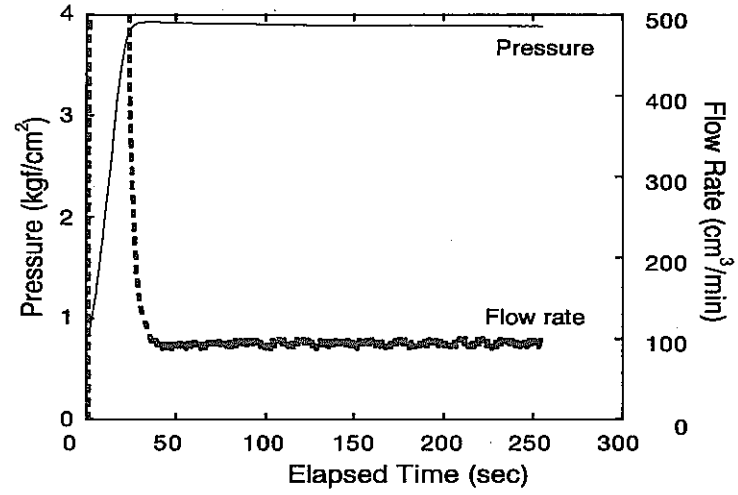

(a) 2-3m

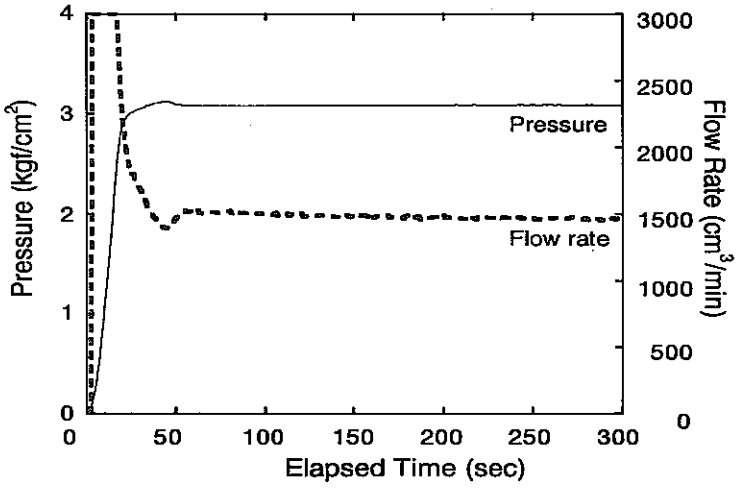

(b) 3-4m

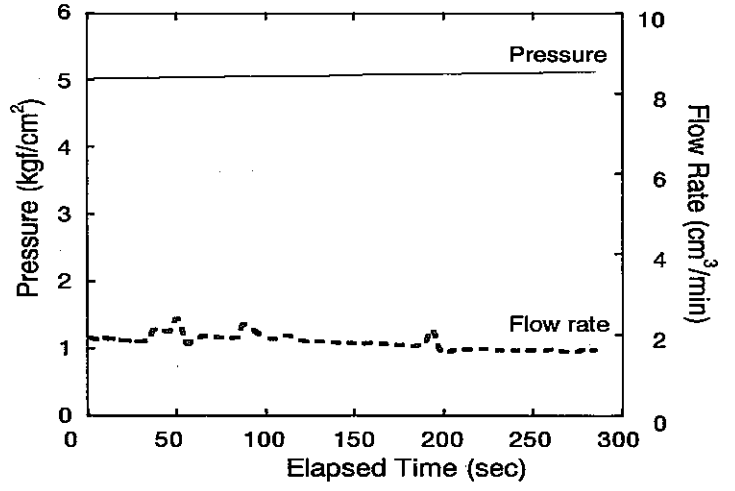

(c) 4-5m

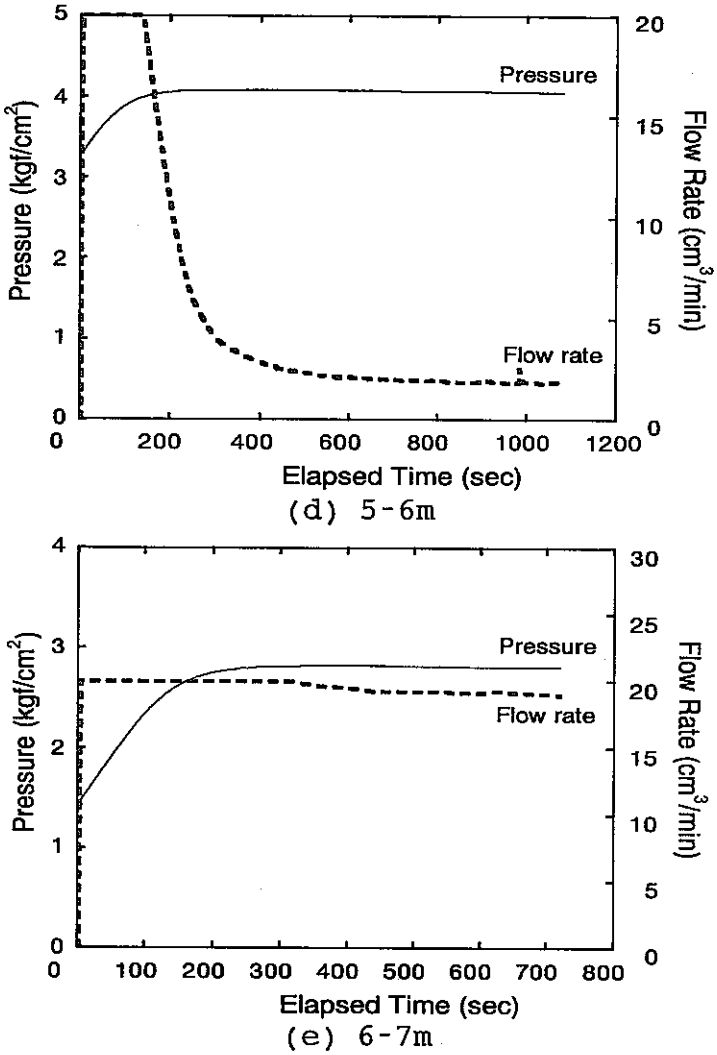

Figure 8 Time history of pressure and flow rate at the injection section(KBH7) Injection test at a constant pressure head

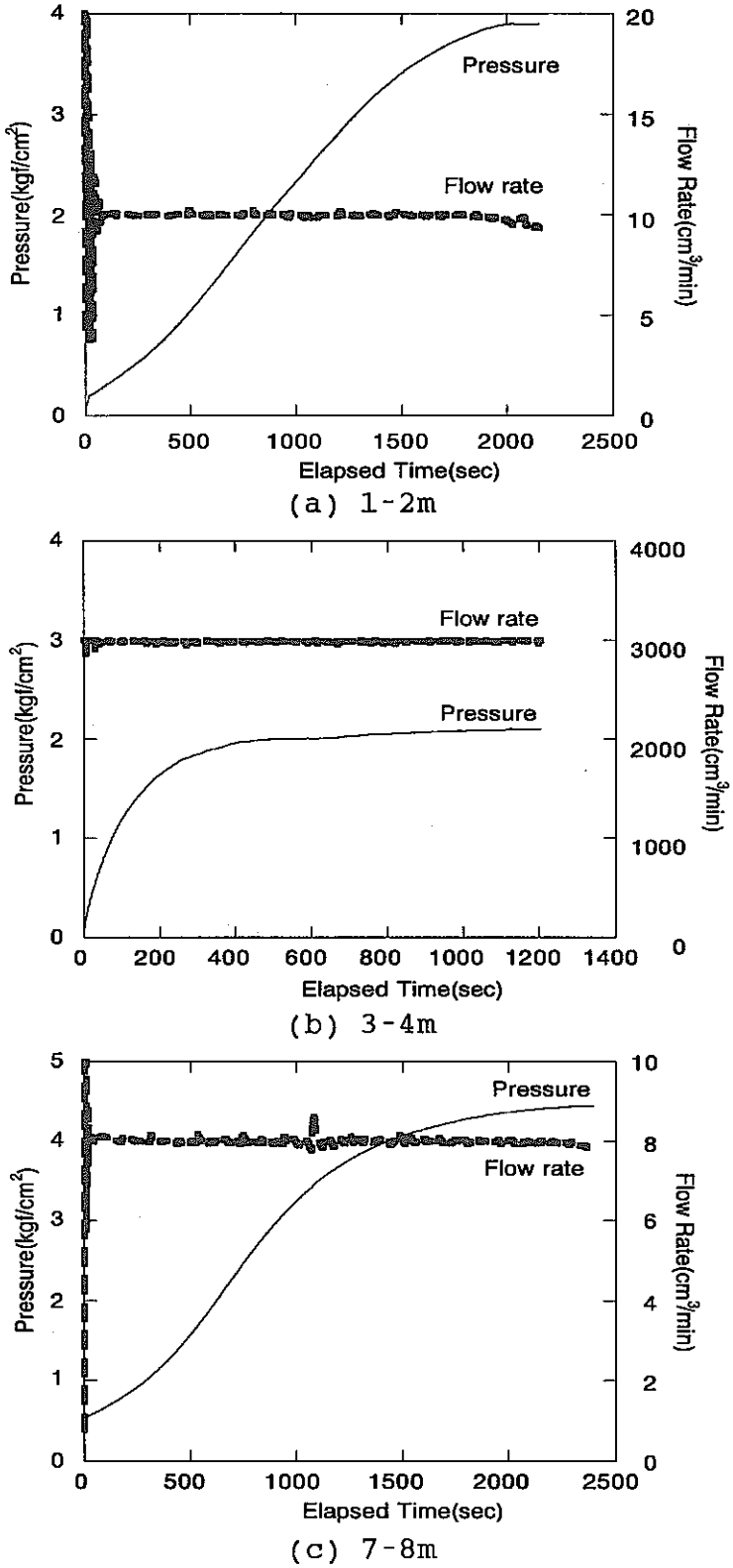

Figure 9 Time history of pressure and flow rate at the injection section(KBH2) Injection test at a constant flow rate

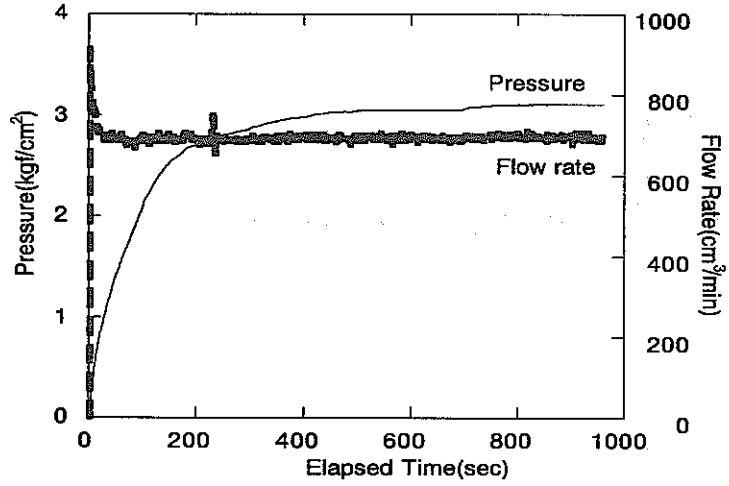

(a) 2-3m

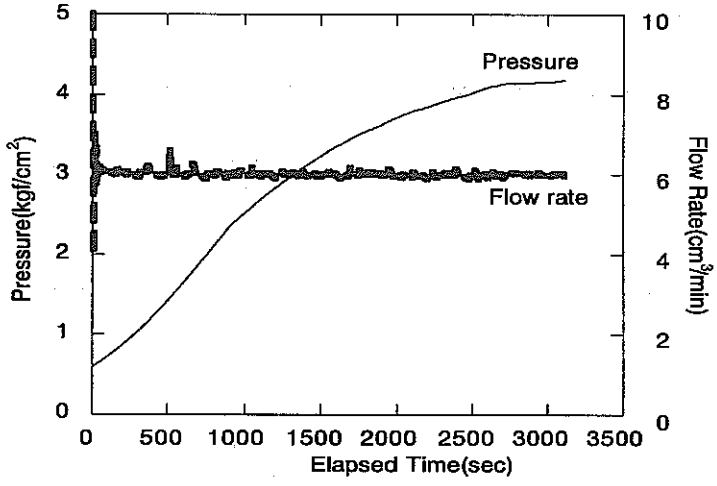

(b) 4-5m

Figure 10 Time history of pressure and flow rate at the injection section(KBH4) Injection test at a constant flow rate

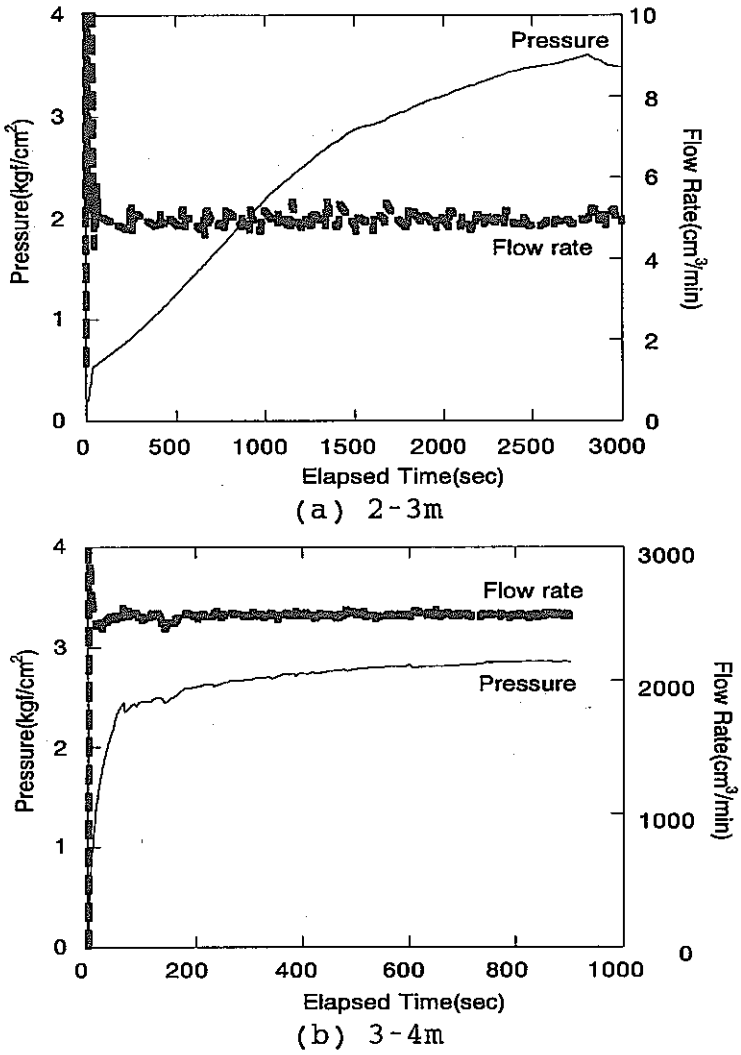

Figure 11 Time history of pressure and flow rate at the injection section(KBH6) Injection test at a constant flow rate

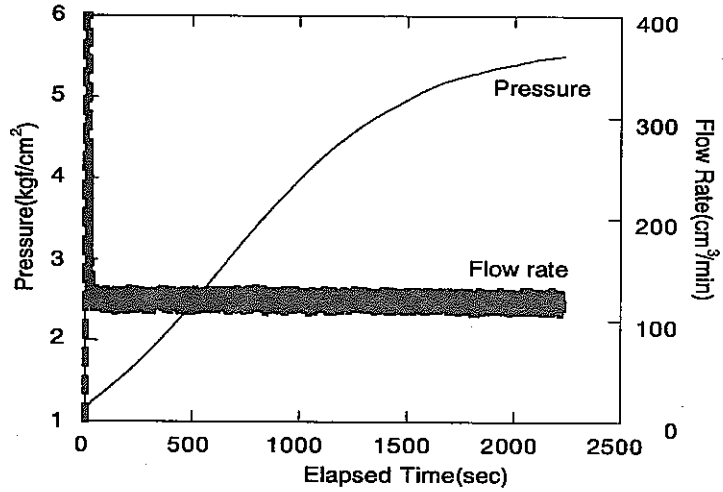

(a) 2-3m

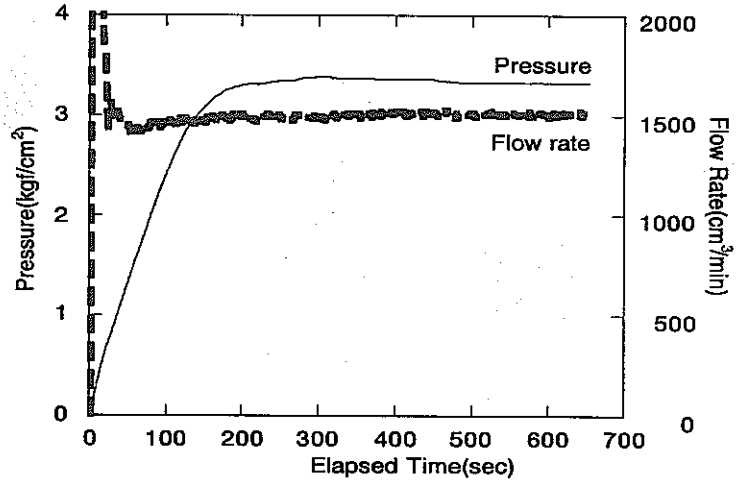

(b) 3-4m

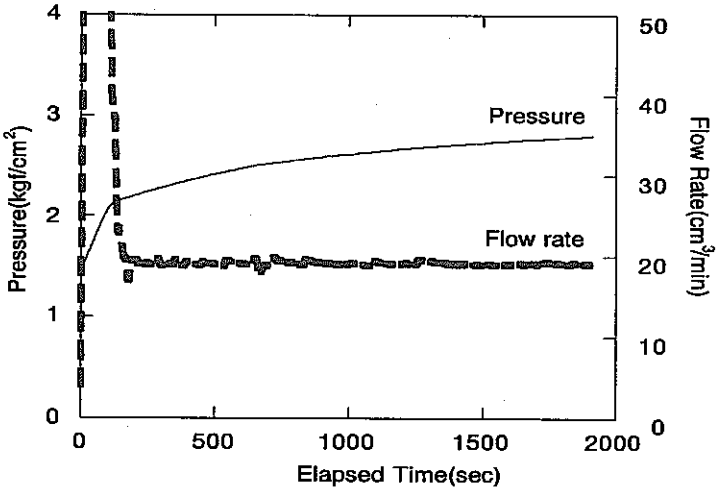

(c) 6-7m

Figure 12 Time history of pressure and flow rate at the injection section(KBH7) Injection test at a constant flow rate

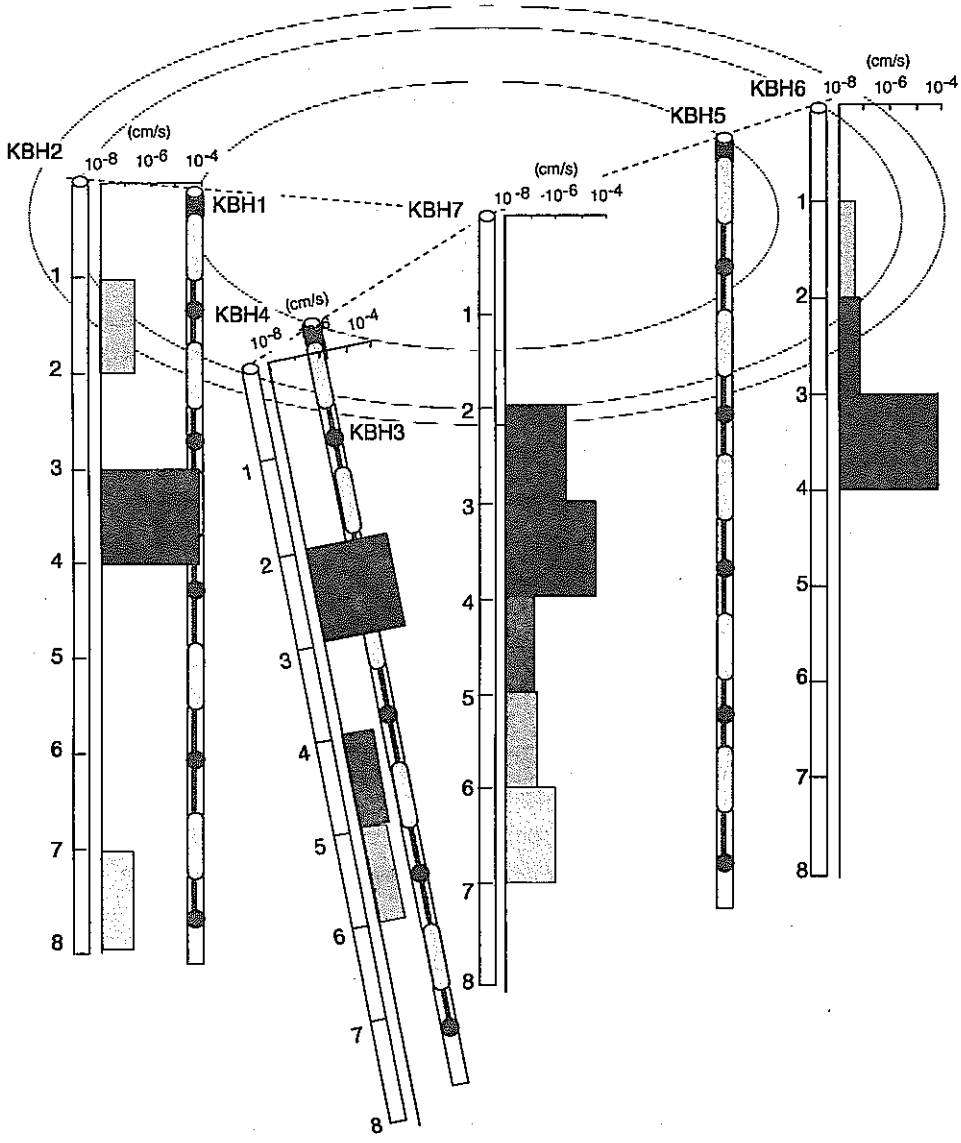

Figure 13 Permeability distribution in the injection boreholes.

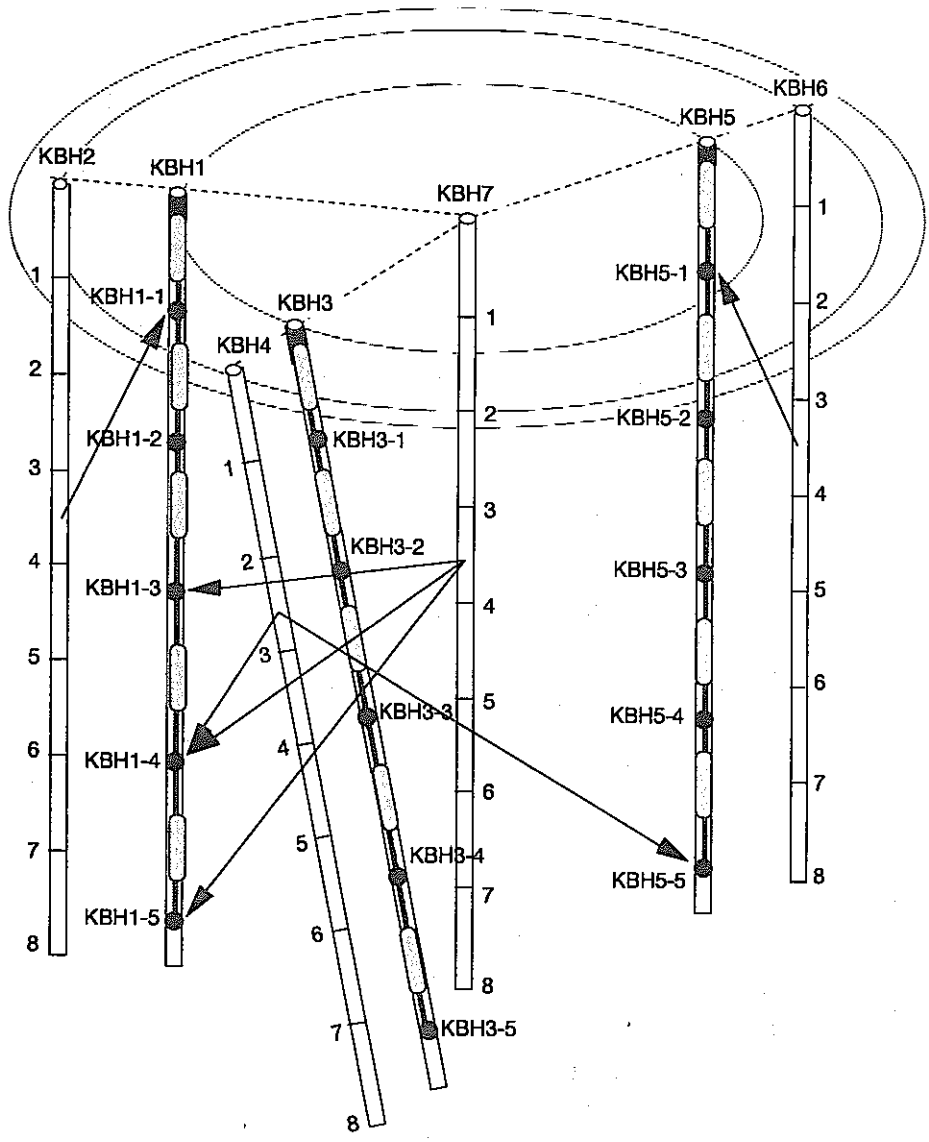

Figure 14 Result of connectivity investigation (TEST 1).

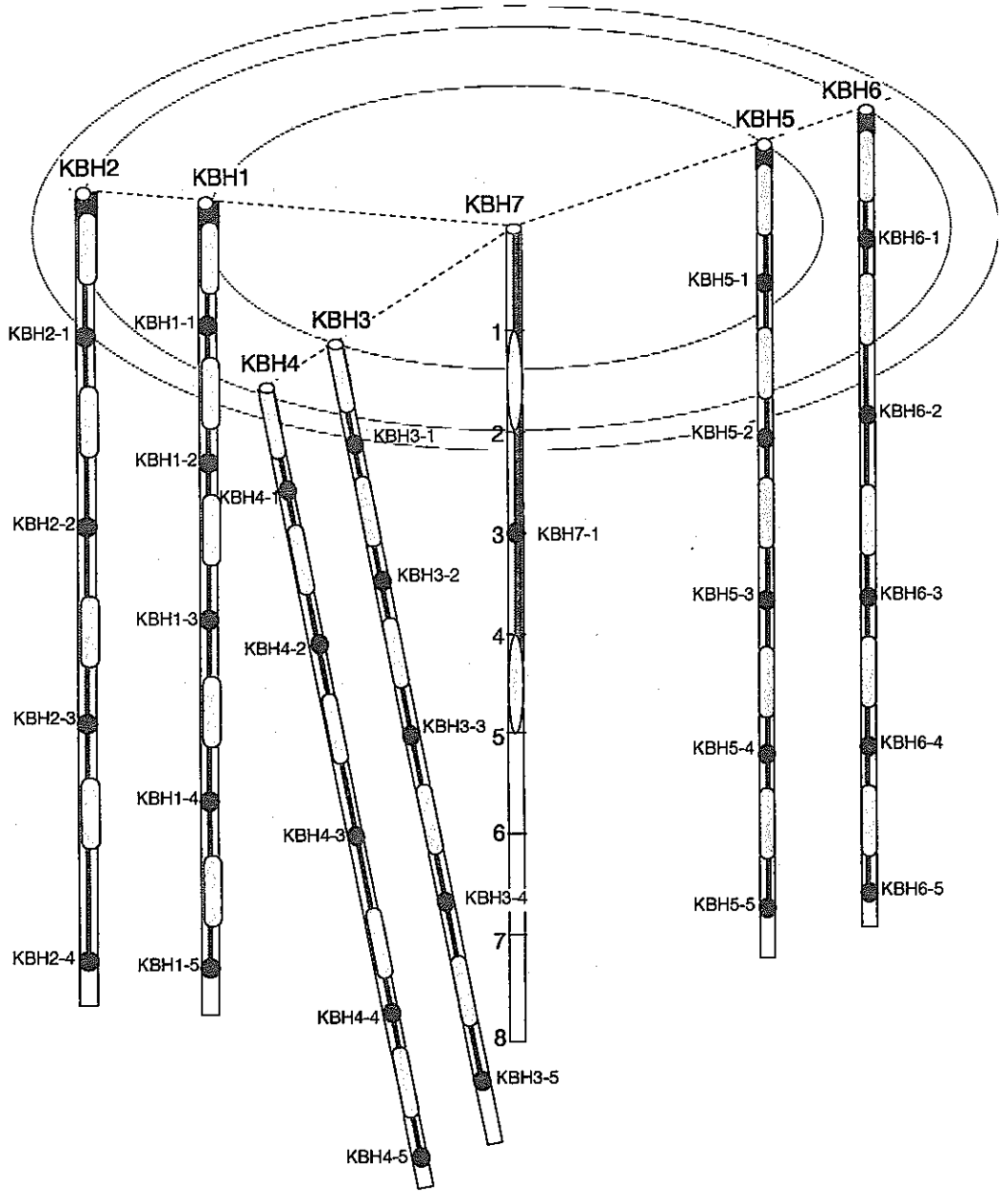

Figure 15 Location of injection/monitoring section (TEST 2).

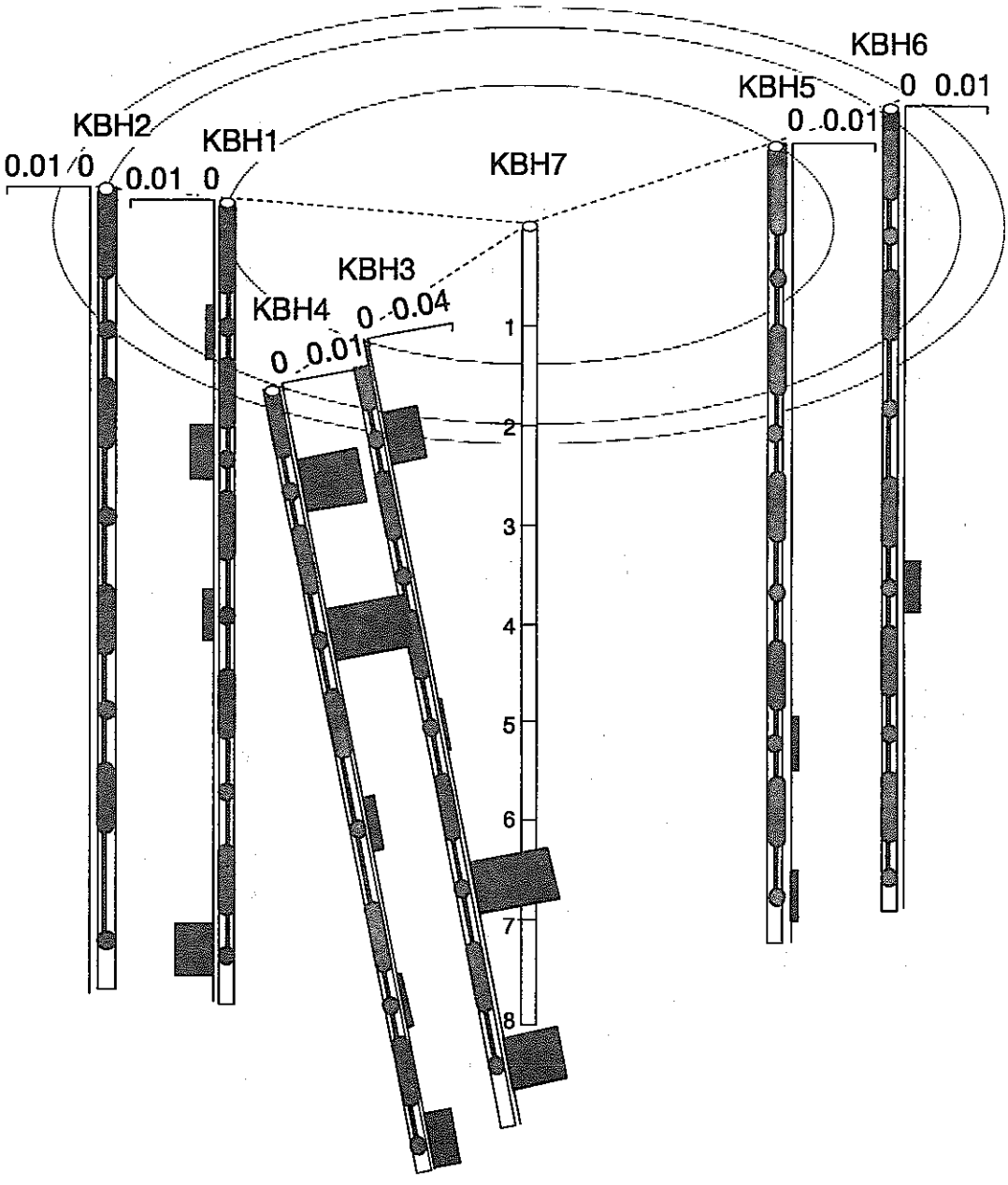

Figure 16 Initial pressure distribution before TEST 2.

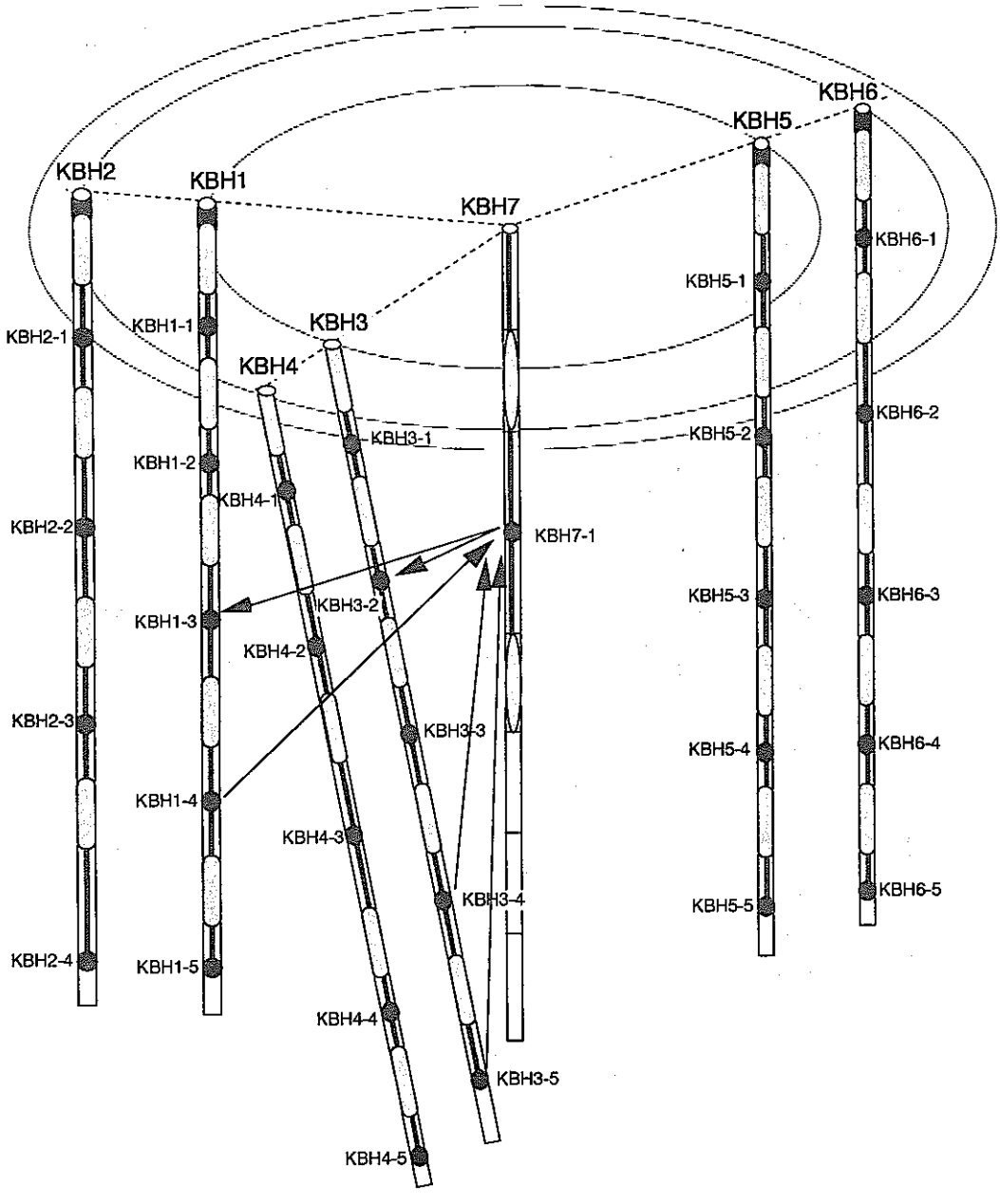

Figure 17 Result of connectivity investigation (TEST2).

4 EXAMINATION OF HYDRAULIC TESTS

4.1 OBJECTIVES

The regime of the ground water flow through rock mass may be very different from the one through porous soil ground because the figure of the void is effected by the cracks or fractures in the rock mass, which derive the strong anisotropy and heterogeneity. Many recent numerical models expressing the flow in the fractured rock mass try to model directly such void structures or to make an equivalent continuum to the fractured permeable rocks. In such models, the fracture observation results are used to introduce the fracture structure in a numerical model. The fracture aperture, which is difficult to measure directly in the field observation, has been calibrated in many cases by using the permeability obtained from the in-situ tests because it is difficult to tell the hydraulically important void from many openings. Moreover it may be difficult to infer accurately the fracture structure in the rock mass by using the limited observation results about the fracture geometry. From above reasons, many uncertainties may remain for discontinuous and continuous modeling approaches as a matter of fact. Moreover, it should be noticed that there is already the concept for the flow field to calculate analytically the permeability from the in-situ tests. Thus, if the analytical model giving the permeability from the in-situ tests is different from the numerical one, the fracture aperture calibrated from such a permeability does not make a correct sense in the model.

To overcome or assist such uncertainties, the general flow model proposed by Barker is used to examine the hydraulic tests in Kamaishi, which considers the flow aspect by the dimension of real number. In the process, the real number dimension is found by fitting the observed results on the type curve of each real number dimension and then the permeability and storativity are calculated for the dimensional model. In this chapter, firstly, the type curve for the constant pressure and flow rate tests are derived briefly on the basis of the Barker's theory. Secondly, the results

at Kamaishi are examined by this theory. The fractional dimension obtained from such a type curve does not have a concrete physical meaning, however this will become the index for the change in the fracture structure introduced by the pressure change and indicate the degree of the anisotropy. Moreover, the correct hydraulic properties matched for the ground status is examined because the observed results will be represented so well by the real number dimension model, whereas the conventional approach used to obtain the permeability from the in-situ tests is assuming some dimension and flow aspect.

It is also recognizable from this theory that the permeability derived from the tests is not inherent as a ground property, but the coefficient in a given flow model. Thirdly, the distribution of the hydraulic properties are examined, which will help to consider the statistical characteristics of the field.

4.2 THEORY

4.2.1 GOVERNING EQUATIONS AND CONDITIONS

The continuity equation of ground water flow in the rock mass from the injection well is given as followings by Barker[5];

$$\frac{1}{\alpha_1}\frac{\partial h}{\partial t} = \frac{1}{r^{n-1}}\frac{\partial}{\partial r}\left(r^{n-1}\frac{\partial h}{\partial r}\right) \qquad (2)$$

where the α_1 is Kf/Ssf, in which Kf is the permeability and Ssf is the specific storage coefficient of the fractured rock mass. n is the real number dimension from 1 to 3, h is the total head in the rock mass and r is the distance from the central point of the injection hole.

The following equation is used to express the skin effect around the injection hole;

$$H = h - S_f r_w \left.\frac{\partial h}{\partial r}\right|_{r=r_w} \tag{3}$$

where S_f is the non dimensional coefficient of skin effect, H is the total head in the injection hole and r_W is the radius of the injection hole.

The conservation equation in the injection hole is given as

$$S_w \frac{\partial H}{\partial t} = Q + K b^{3-n} \alpha_n r_w^{n-1} \left.\frac{\partial h}{\partial r}\right|_{r=r_w} \tag{4}$$

where S_W is the storage capacity of the source which is given as πr_W^2, Q is the injection rate. α_n is given as

$$\alpha_n = \frac{2\pi^{n/2}}{\Gamma(n/2)} \tag{5}$$

where Γ is the gamma function. $b^{3-n} \alpha_n r_W^{n-1}$ implies the area through which the injected water goes in n dimensional way. Thus, this dimension is $[L]^2$. This is the point of Barker's theory. Figure 18 shows the schematic view of the area given by this equation with some specific values of n..

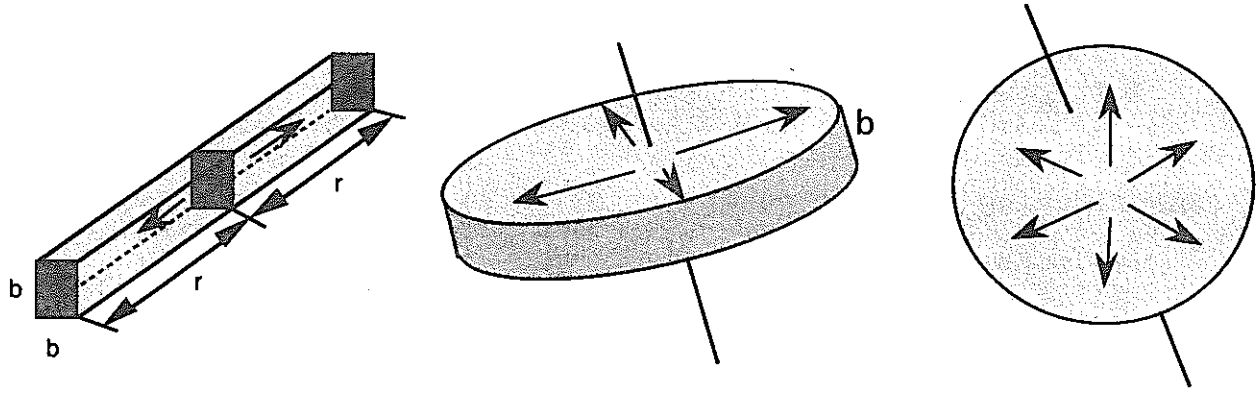

a) 1 dimension b) 2 dimension c) 3 dimension

Figure 18 Schematic view of the flow area for different dimensional model

A boundary condition is introduced which states the heat is zero at infinite distance from the source.

$$h(\infty,t)=0 \tag{6}$$

The boundary condition at the source is given as

$H=H_0$ for constant pressure test

$Q=Q_0$ for constant flow rate test (7)

It will normally be assumed that the initial condition is that the head is zero through the system.

$$h(r,0)=H(0)=0 \tag{8}$$

4.2.2 DERIVATION OF TYPE CURVE OF CONSTANT PRESSURE TEST

The following non dimensional parameters are defined:

$$h_D=\frac{h}{H_0} \tag{9}$$

$$t_D=\frac{\alpha_1 t}{r_w^2} \tag{10}$$

$$r_D=\frac{r}{r_w} \tag{11}$$

$$Q_D=\frac{Q}{K_f b^{3-n}\alpha_n r_w^{n-1}} \tag{12}$$

Substituting into the equations (2), (3) and (4), we obtain

$$\frac{\partial h_D}{\partial t}=\frac{n-1}{r_D}\frac{\partial h_D}{\partial r_D}+\frac{\partial^2 h_D}{\partial {r_D}^2} \tag{13}$$

$$H_D=h_D-S_f\frac{\partial h_D}{\partial r_D}\bigg|_{r_D=1} \tag{14}$$

$$\beta\frac{\partial H_D}{\partial t_D}=Q_D+\gamma\frac{\partial h_D}{\partial r_D}\bigg|_{r_D=1} \tag{15}$$

where β is $\pi H0/(S_{sf} b^{3-n} \alpha_n r_W^{n-1})$, γ is $H0/r_W$.

Laplace transforms is used successfully to solve the equations. The subsidiary equations are:

$$\overline{h_D}p = \frac{n-1}{r_D}\frac{\partial \overline{h_D}}{\partial r_D} + \frac{\partial^2 \overline{h_D}}{\partial r_D^2} \tag{16}$$

$$\overline{H_D} = \overline{h_D} - S_f \left.\frac{\partial \overline{h_D}}{\partial r_D}\right|_{r_D=1} \tag{17}$$

$$\beta \overline{H_D}p = \overline{Q_D} + \gamma \left.\frac{\partial \overline{h_D}}{\partial r_D}\right|_{r_D=1} \tag{18}$$

The transformed boundary condition at the source is

$$\overline{H_D} = \frac{1}{p} \quad . \tag{19}$$

The general solutions for the equation (16) is of the form:

$$\overline{h_D} = C(p) r_D^{\nu} K_{\nu}(\sqrt{p} r_D) + D(p) r_D^{\nu} I_{\nu}(\sqrt{p} r_D) \tag{20}$$

where I_ν and K_ν are modified Bessel functions of nth order of the first and second kind, respectively. n is 1-n/2. The coefficient $C(p)$ in the equation (20) is found to be nil since the restricted boundary condition:

$$\lim_{r_D \to \infty} \overline{h_D} = 0 \tag{21}$$

So the general solution in this case is given as

$$\overline{h_D} = C(p) r_D^{\nu} K_{\nu}(\sqrt{p} r_D) \tag{22}$$

The derivative of the above equation at the surface of the source is written as

$$\frac{\partial \overline{h_D}}{\partial r_D} = -C(p) r_D^{\nu} \sqrt{p} K_{\nu-1}(\sqrt{p} r_D) \tag{23}$$

Substituting the equations (22) and (23), the equation (14) is rewritten as

$$\overline{H_D} = C(p)\left(K_\nu(\sqrt{p}) + S_f\sqrt{p}K_{\nu-1}(\sqrt{p})\right) \tag{24}$$

from which the function $C(p)$ is determined.

Substituting the equations (22), (23) and $C(p)$ from (24), the equation (15) is given as

$$\overline{Q_D} = \overline{H_D}\left\{\beta p + \gamma\frac{\sqrt{p}K_{\nu-1}(\sqrt{p})}{K_\nu(\sqrt{p}) + S_f\sqrt{p}K_{\nu-1}(\sqrt{p})}\right\} \tag{25}$$

The transformed boundary condition (19) is applicable to the above equation. Finally, the transformed injection flow rate is given as

$$\overline{Q_D} = \frac{1}{p}\left\{\beta p + \gamma\frac{\sqrt{p}K_{\nu-1}(\sqrt{p})}{K_\nu(\sqrt{p}) + S_f\sqrt{p}K_{\nu-1}(\sqrt{p})}\right\} \tag{26}$$

By using a numerical Laplace inversion technique, the Q_D as a function of time is obtained for any dimension. In this case, the numerical inversion scheme introduced by Stehfest[6] is used, of which accuracy was confirmed by Karasaki[7]. The validation of the results in this case are examined by comparing with the flow rate at the steady state. The steady injection flow rate of the constant pressure test is obtained like following for dimensions greater than two:

$$H_{t=\infty} = \frac{-Q_{t=\infty}\Gamma(1-\nu)r_w^{2\nu}(1-2\nu S_f)}{4\pi^{1-\nu}K_f b^{3-n}\nu} \tag{27}$$

By using the definition of α_n, Q_D and γ, the above equation is rewritten with the non dimensional parameters as

$$Q_D = \frac{2\gamma\nu}{1-2\nu S_f} \tag{28}$$

By comparison of this value with the Q_D obtained from the equation (26) at the large t_D, it is examined if the numerical Laplace inversion is successfully completed.

Substituting $C(p)$ of the equation (24) into the equation (22) and applying the boundary condition of the equation (19), the transformed head in the rock mass is given as

$$\overline{h_D} = \frac{r_D^{\nu} K_{\nu}(\sqrt{p} r_D)}{p\left\{K_{\nu}(\sqrt{p}) + S\sqrt{p} K_{\nu-1}(\sqrt{p})\right\}} \tag{29}$$

The behavior of the head at the observed well during the constant pressure test is examined with this equation.

4.2.3 DERIVATION OF TYPE CURVE OF CONSTANT FLOW RATE TEST

In this case, the following dimensionless parameters are defined as used in the usual well problem:

$$h_D = \frac{K b^{3-n} \alpha_n r_w^{n-1}}{Q_0 r_w}\left(h_i - h\right) \tag{30}$$

$$H_D = \frac{K b^{3-n} \alpha_n r_w^{n-1}}{Q_0 r_w}\left(H_i - H\right) \tag{31}$$

$$Q_D = \frac{Q}{Q_0} \tag{32}$$

It will normally be assumed that the initial head is zero throughout the system. So h_i =0 and H_i = 0. It would be understood from the equations (30) and (31) that the dimensionless parameters h_D and H_D in this case imply the dimensionless drawdown in the rock mass and at the source, respectively.

Substituting the equations (30) and (31) into the equations (2) and (3), the same equations to the equations (16) and (17) is

obtained. For the equation (4), the following equation with the dimensionless parameters are obtained:

$$\eta\frac{\partial H_D}{\partial t_D}=-Q_D+\left.\frac{\partial h_D}{\partial r_D}\right|_{r_D=1} \tag{33}$$

where $\eta = \pi r_w/S_s b^{3-n}\alpha_n r_w^{n-1}$. The equations (23), (24) and (25) hold in this case. Substituting these equations into the subsidiary equation of (33), the transformed dimensionless head at the source is given as

$$\overline{H_D}=-\overline{Q_D}\left(\eta p+\frac{\sqrt{p}K_{\nu-1}(\sqrt{p})}{K_\nu(\sqrt{p})+S_f\sqrt{p}K_{\nu-1}(\sqrt{p})}\right)^{-1} \tag{34}$$

The transformed boundary condition of the equation (7) for the constant flow rate test are applied to the above equation. The final form of the transformed dimensionless head at the source is written as

$$\overline{H_D}=-\frac{1}{p}\left(\eta p+\frac{\sqrt{p}K_{\nu-1}(\sqrt{p})}{K_\nu(\sqrt{p})+S_f\sqrt{p}K_{\nu-1}(\sqrt{p})}\right)^{-1} \tag{35}$$

By using the numerical Laplace inversion scheme, the type curve for the constant flow rate test is obtained.

4.3 TYPE CURVES OF CONSTANT PRESSURE AND FLOW RATE TESTS

4.3.1 CONSTANT PRESSURE TESTS

Figure 19 shows several log-log plots of Q_D and t_D for some dimensions, which is the type curves of the constant pressure test with β of 5.28×10^6 and γ of 132. The skin effect, S_f, is set to be zero. While this curve is not sensitive for the value of β, the curve moves vertically according to the value of γ. In order to apply this curve for a constant pressure test, the value of γ has

to be firstly identified from the applied head, H_0, and the radius of the injection hole, r_w. The type curves for some dimensions are made in terms of the value of γ and the dimension is identified by fitting the log-log plots of the observed Q and t to the type curves. From the matching point, the permeability, K_f, is calculated with the equation (12) by using the value of β and α_n which is calculated from the dimension, n, with the equation (5). S_{sf} is evaluated from K_f, t_D, t and r_w with the equation (10).

4.3.2 CONSTANT FLOW RATE TESTS

Figure 20 shows the several log-log plots of H_D and t_D with η of 100 for some dimensions. This curve is dependent on the value of η. Thus, fitting process with log-log plot of the measured H and t would be carried out with the type curves for some values of η and then the best fitting curve has to be found. This process would be programmed in the computer code. Similarly to the process in the case of the constant pressure test, K_f is calculated through the values of H_D and H of the matching point for the best fitted curve of the dimension, n, and then S_{sf} is evaluated in terms of K_f, t_D, t and r_w .

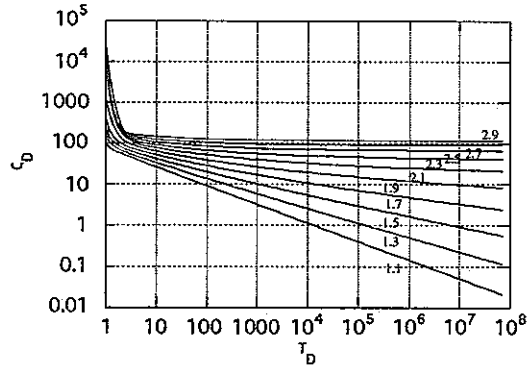

Figure 19 Constant pressure test

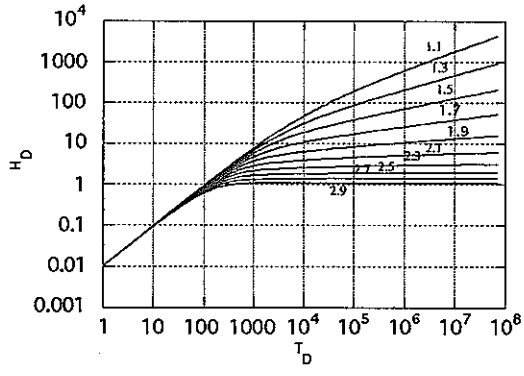

Figure 20 Constant flow rate test

4.4 EXAMINATION OF KAMAISHI IN-SITU TESTS

4.4.1 SINGLE BOREHOLE TESTS

In Kamaishi area, the constant pressure and flow rate tests were carried out by using four boreholes, KBH1, 3, 5 and 7. The above method applied to those tests and Table 3 shows the results for the constant pressure tests. Table 4 shows the results for the constant flow rate tests. The results of the constant flow rate tests were difficult to fit to the type curve because the pressure in the injection section rose in a different way from the ideal way assumed in the analytical method. Thus, the number of the boreholes are limited for the examination. The results obtained by the examination are, however, similar to the ones for the constant pressure results. Therefore, the consideration about the hydraulic properties is carried out by mainly using the constant pressure test results.

The geometric mean of the permeability from the constant pressure tests, which were injected by the same pressure of 3 kg/cm^2, is 2.5×10^{-9} m/s and the standard deviation of $\ln(K)$ is 3.1. The distribution of the permeability is assumable to be lognormal one as shown in Figure 21. The average of the dimension is 2.2 and the standard deviation is 0.46. The distribution of the dimension is assumable to be normal one as shown in Figure 22.

Figure 23 shows the autocorrelation coefficient of the permeability as a function of distance, x, from which the correlation length, λ, is estimated by assuming the distribution as the exponential function, i.e., $\eta e^{-x/\lambda}$. η should be less than 1 which is corresponding to the nugget effect of zero. It is found from Figure 23 that the correlation length is 1.54m and η is 0.0182. η is very high, which means the big nugget effect. However, this high η is derived from the large variance of the data at the distance of 1m which is the minimum distance between measuring points. If the nugget effect is assumed to be zero, i.e. η of 1, the correlation length become 0.624m. Anyway, the correlation

length of the permeability is very short. Figure 24 shows the autocorrelation length of the dimension as a function of distance. As similar to the permeability, if η is assumed to be 1, the correlation length of the dimension is 0.57m, which is also very short. This means that the hydraulic property and flow aspect are drastically changing at a short distance. Thus, it may be said that the heterogeneity and anisotropy of the flow filed are very high in this area.

In the constant pressure tests, the injection pressure was raised step by step at sections KBH2;3, KBH4;2 and KBH6;3. The examination results for the pressure increasing tests are summarized in Table 5. Figure 25, 26 and 27 show the relations of the pressure with the permeability and the dimension. It is seen from those figures that the permeability is increasing with pressure and the peak value exists during pressure increasing process. Moreover, it is found that the dimension is increasing for all cases. When the dimension is high, the permeability is estimated as a low value even if the same flow rate is observed for some injection pressure. Thus, the existence of the peak of the permeability is relating to the dimension increasing process. These results may be useful to make a model considering the mechanical coupling with flow problem.

Table 3 Results of the constant pressure tests

Section	Dimension	*Kf* (m/s)	*Sf* (1/m)	*Kf*/*Sf* (m^2/s)
KBH2;1	1.3	1.17E-09	1.25E-06	9.36E-04
KBH2;3	2.6	1.18E-05	3.75E-04	3.15E-02
KBH2;5	2.1	8.85E-11	6.78E-07	1.31E-04
KBH2;7	2.1	1.83E-09	4.06E-06	4.51E-04
KBH4;1	2.1	3.67E-10	2.81E-06	1.31E-04
KBH4;2	2.1	1.76E-07	6.50E-04	2.71E-04
KBH4;3	2.9	6.22E-10	1.29E-05	4.82E-05
KBH4;4	2.3	1.95E-09	1.24E-05	1.57E-04
KBH4;5	2.1	4.05E-10	2.10E+00	1.93E-10
KBH4;6	2.1	2.80E-10	1.34E-06	2.09E-04
KBH6;1	1.1	2.12E-10	7.82E-07	2.71E-04
KBH6;2	2.1	8.04E-10	5.94E-06	1.35E-04
KBH6;3	2.9	2.50E-06	3.88E-02	6.44E-05
KBH6;4	2.6	6.77E-11	2.18E-06	3.11E-05
KBH7;1	2.9	4.29E-07	3.17E-03	1.35E-04
KBH7;2	2.1	1.65E-06	2.70E-14	6.11E+07
KBH7;4	2.6	3.77E-10	1.27E-04	2.97E-06
KBH7;5	2.1	3.64E-10	2.25E-05	1.62E-05
KBH7;6	2.9	4.34E-08	1.27E-04	3.42E-04
KBH7;7	2.1	2.13E-10	1.70E-05	1.25E-05

Table 4 Results of the constant flow rate tests

Section	Dimension	*Kf* (m/s)	*Sf* (1/m)	*Kf*/*Sf* (m^2/s)
KBH2;1	1.1	2.76E-08	3.81E-06	7.24E-03
KBH2;3	2.2	6.78E-05	4.36E-02	1.56E-03
KBH2;7	1.8	4.03E-09	1.47E-05	2.74E-04
KBH4;2	1.9	6.22E-07	8.57E-04	7.26E-04
KBH4;4	1.4	5.87E-10	8.62E-05	6.81E-06
KBH6;2	1.7	1.40E-09	1.79E-04	7.82E-06
KBH6;3	1.2	1.44E-06	3.96E-04	3.64E-03
KBH7;2	2.6	5.56E-07	1.28E-04	4.34E-03
KBH7;3	1.8	1.70E-06	3.53E-03	4.82E-04
KBH7;6	1.8	2.26E-08	7.83E-06	2.89E-03

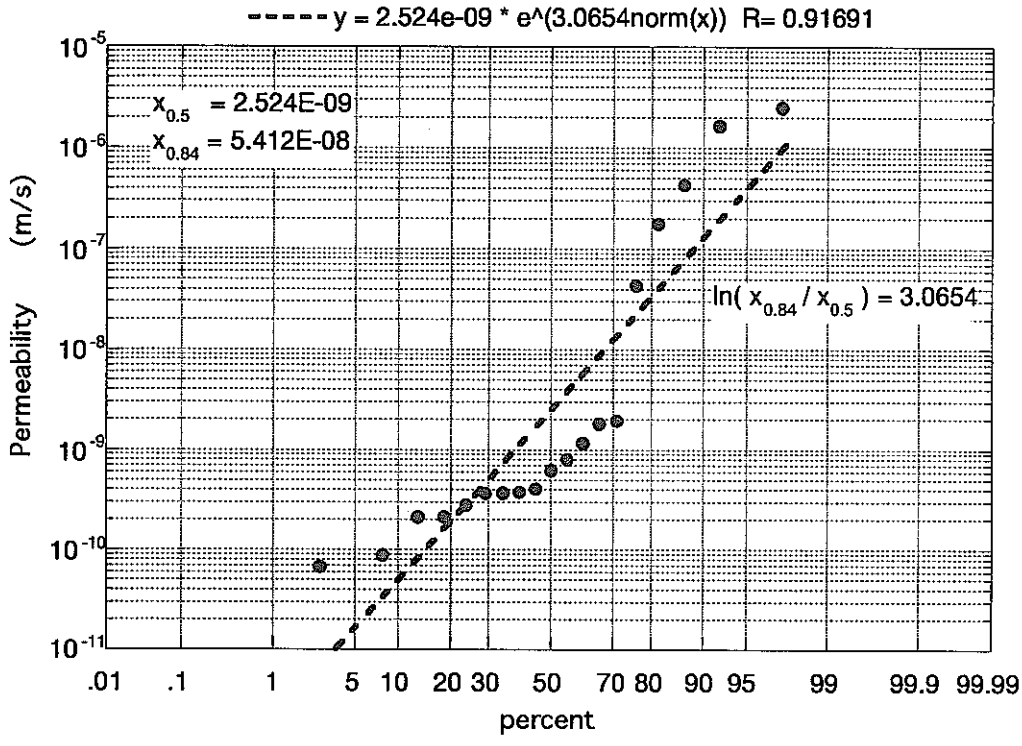

Figure 21 Probability of the permeability

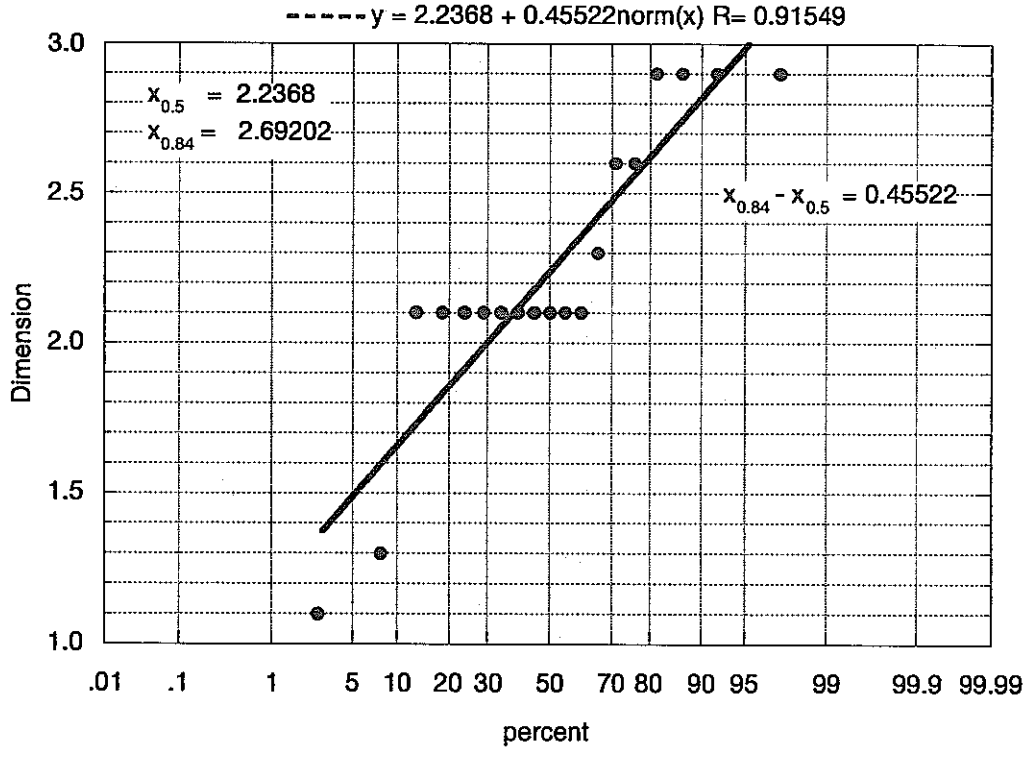

Figure 22 Probability of the dimension

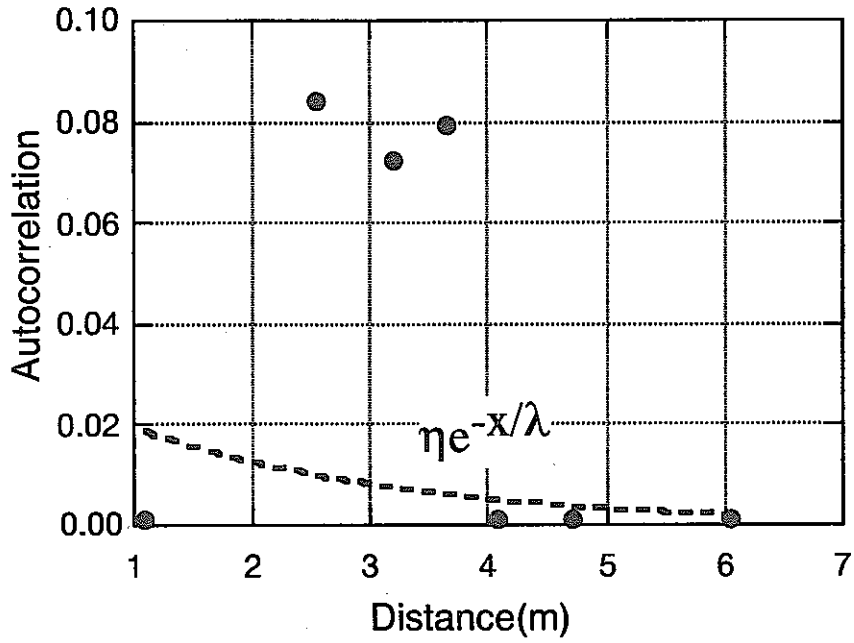

Figure 23 Autocorrelation coefficient of the permeability as a function of distance

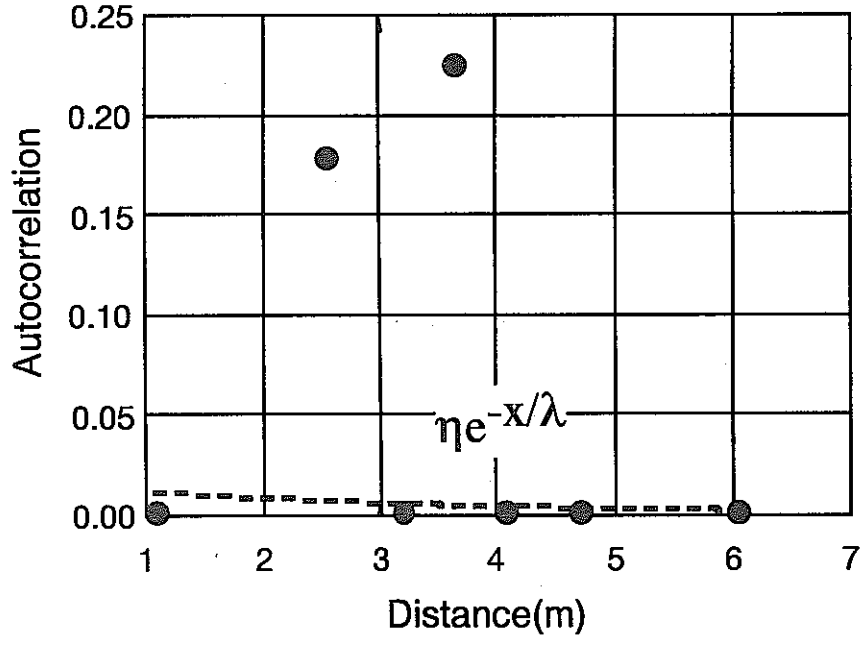

Figure 24 Autocorrelation length of the dimension as a function of distance

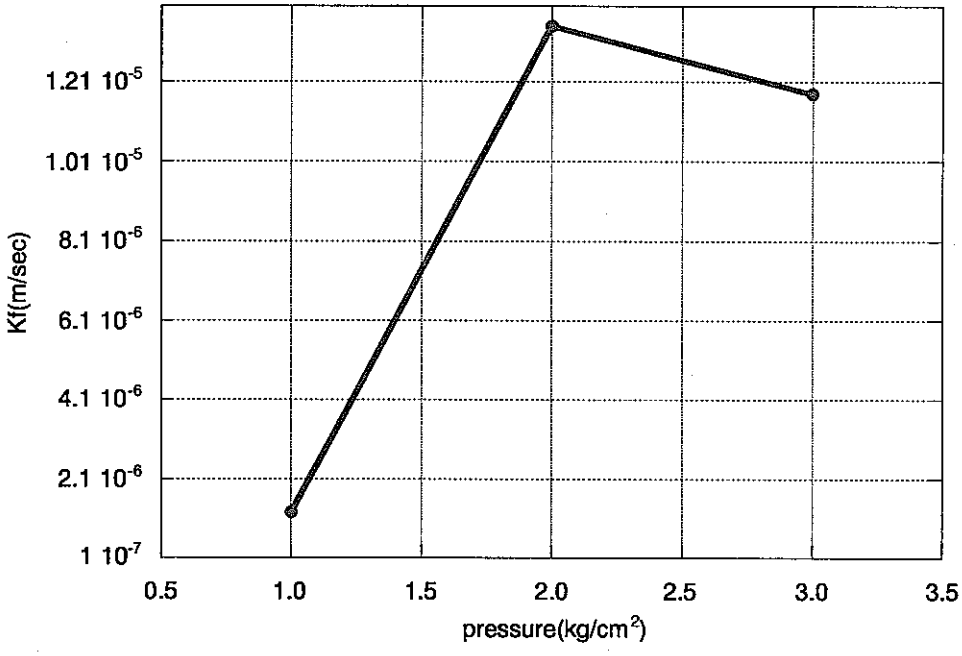

(a) Permeability as a function of pressure

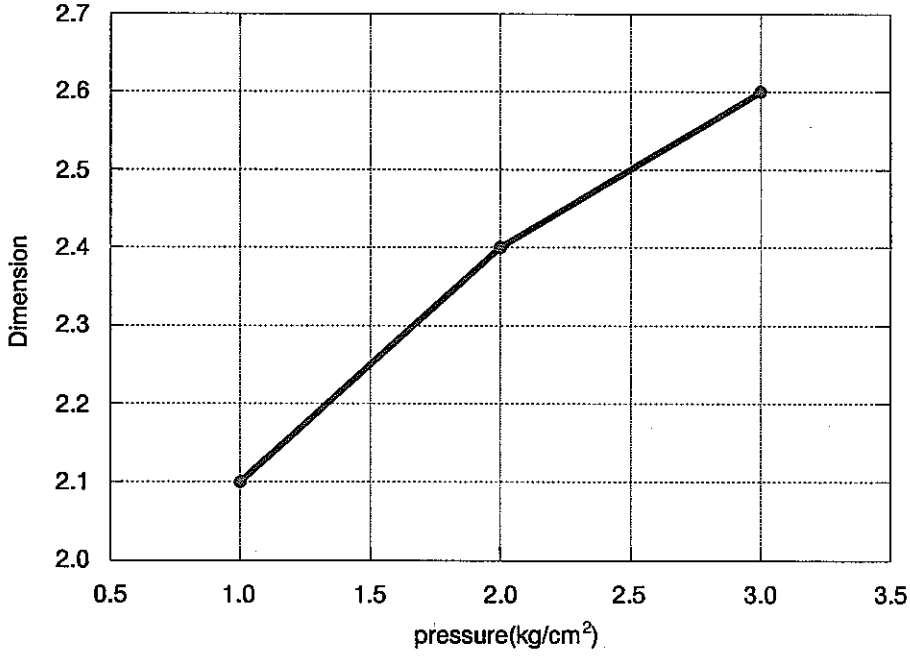

(b) Dimension as a function of pressure

Figure 25 Relation of the pressure with the permeability and the dimension at KBH2;3(3-4m)

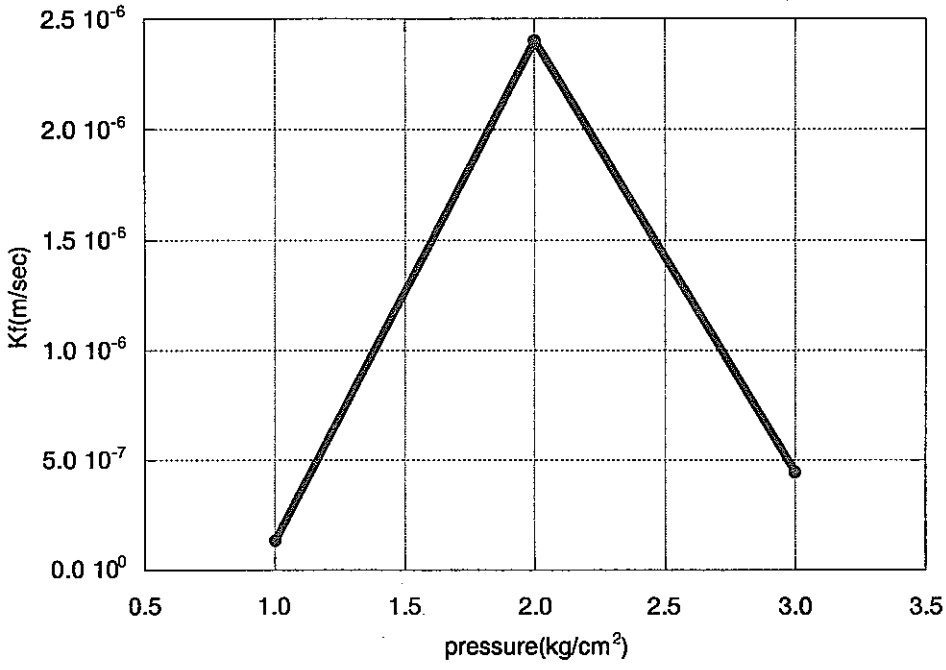

(a) Permeability as a function of pressure

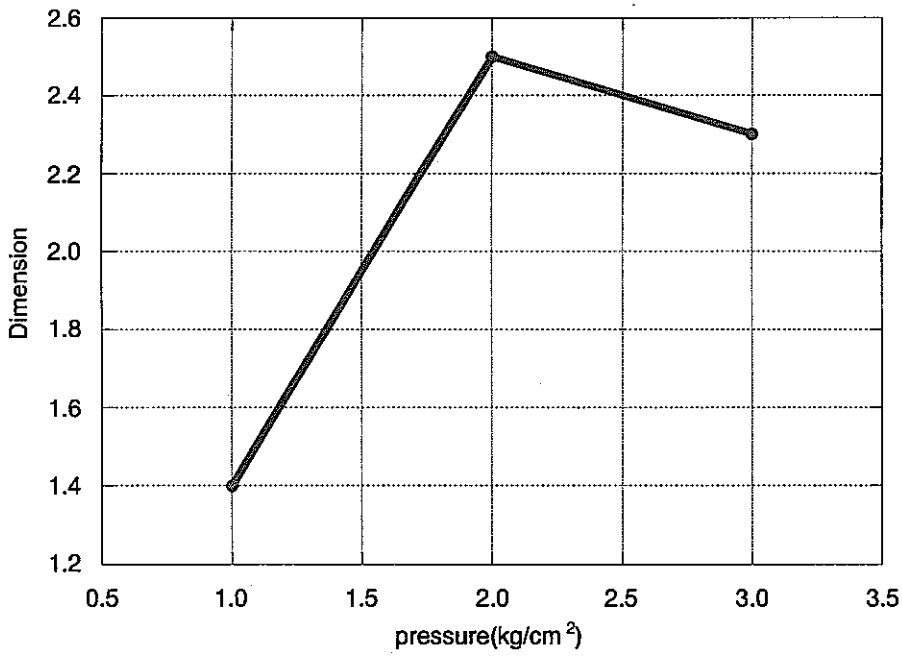

(b) Dimension as a function of pressure

Figure 26 Relation of the pressure with the permeability and the dimension at KBH4;2(2-3m)

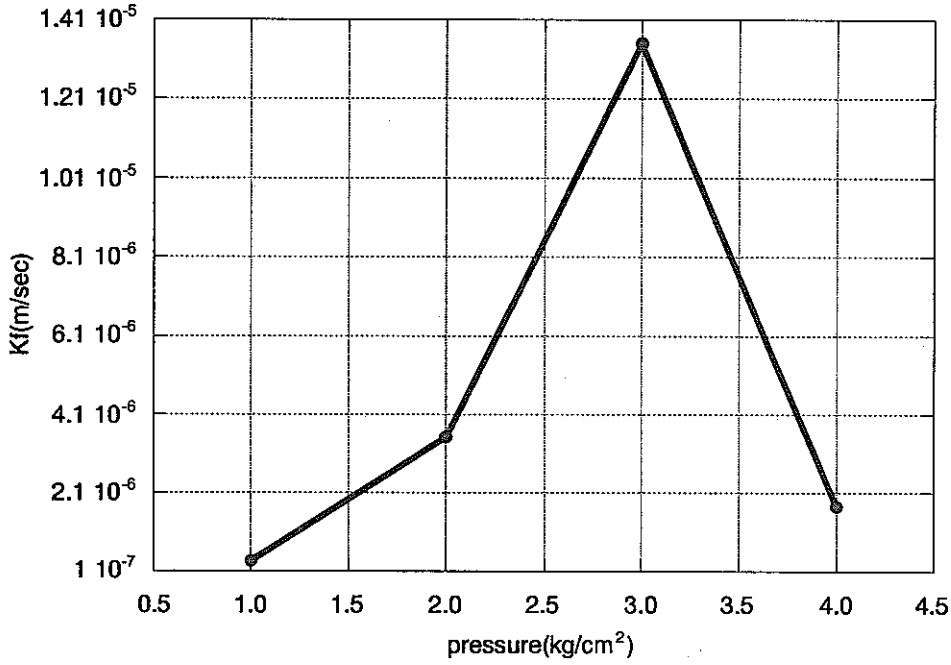

(a) Permeability as a function of pressure

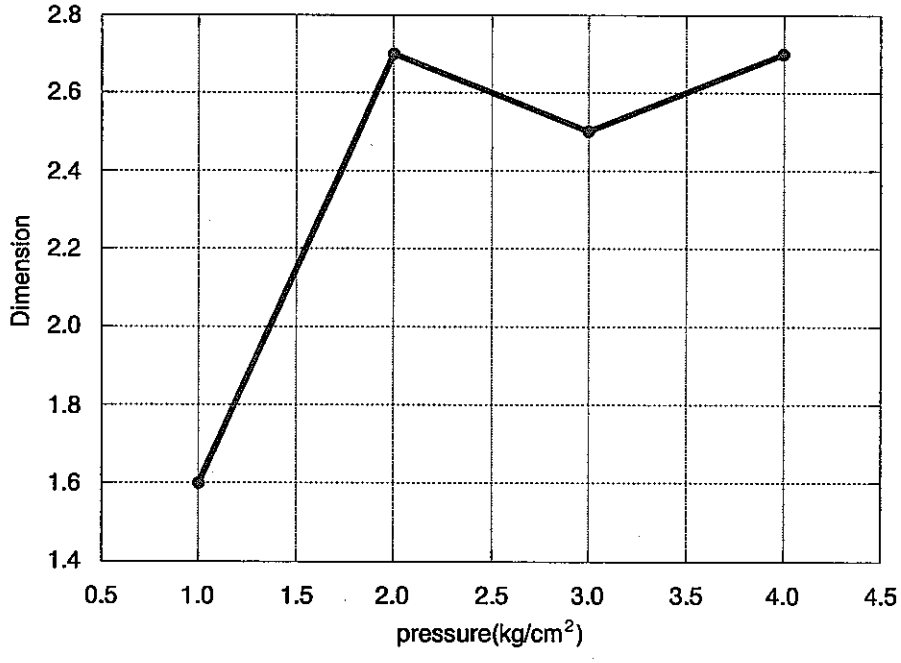

(b) Dimension as a function of pressure

Figure 27 Relation of the pressure with the permeability and the dimension at KBH6;3(3-4m)

Table 5 Results of pressure increasing tests

Section	Pressure (kgf/cm^2)	Dimension	Kf (m/s)	Sf (1/m)	Kf/Sf (m^2/s)
KBH2;3	1.0	2.1	1.26E-06	7.25E-03	1.74E-04
	2.0	2.4	1.35E-05	1.55E-01	8.71E-05
	3.0	2.6	1.18E-05	3.75E-04	3.15E-02
KBH4;2	1.0	1.4	1.36E-07	5.52E-04	2.46E-04
	2.0	2.5	4.29E-06	7.76E-01	5.53E-06
	3.0	2.3	4.46E-07	2.03E-09	2.20E+02
KBH6;3	1.0	1.6	3.63E-07	1.01E-03	3.59E-04
	2.0	2.7	3.53E-06	2.52E-01	1.40E-05
	3.0	2.5	1.35E-05	2.98E-01	4.53E-05
	4.0	2.7	1.75E-06	9.14E-07	1.91E+00

4.4.2 INTERFERENCE TESTS

During the hydraulic tests using single borehole, the pressure changes were observed at boreholes KBH1, 3 and 5. Among tests, the pressure changes were clearly observed at a few boreholes in the constant flow rate tests. Those tests also become the interference tests. The examination results of the interference tests are summarized in Table 6, in which 7 observations are analyzed. Figure 28 shows the comparison of the permeability between injection and observation sections. It is found from this figure that the hydraulic conductivities examined at the observation section are larger than the one at the injection section. Figure 29 shows the same relation about the dimension. It is found in this case that the dimension does not have clear relation between observation and injection sections. The permeability at the observation section may reflex the flow paths between two boreholes while the one at the injection section may be effected

by the paths in the more larger region. The dimension may represent the average flow aspect in such a region. Since the dimension does not have clear tendency between injection and observation section, the way to flow might not be dependent on the volume of the flow region. On the contrast, the permeability may be influenced by the volume of the flow region.

Table 6 Results of interference tests

Injection section		KBH2;3	KBH4;2		KBH6;3	KBH7;3		
Observed section		KBH1-1	KBH1-4	KBH5-5	KBH5-1	KBH1-3	KBH1-4	KBH1-5
Distance(m)		2.172	4.383	6.056	2.242	1.642	2.932	4.486
Unit direction vector	X	-0.0548	-0.3482	-0.4919	0.2252	0.2259	0.1265	0.0827
	Y	0.2192	-0.4280	0.0761	-0.1708	-0.8642	-0.4840	-0.3163
	Z	0.9742	-0.8339	-0.8339	0.9594	-0.4501	-0.8660	-0.9449
b (m)		1.0	1.0	1.0	1.0	1.0	1.0	1.0
Qo (m^3/s)		0.18	0.042	0.042	0.15	0.09	0.09	0.09
Dimension		2.9	2.1	2.9	2.6	1.1	1.4	1.1
Kf (m/s)		6.98E-05	1.19E-05	1.11E-05	6.53E-06	4.58E-04	1.80E-04	4.12E-05
Sf (1/m)		1.07E-03	2.94E-03	6.07E-04	1.50E-03	1.06E-02	3.12E-02	1.51E-02

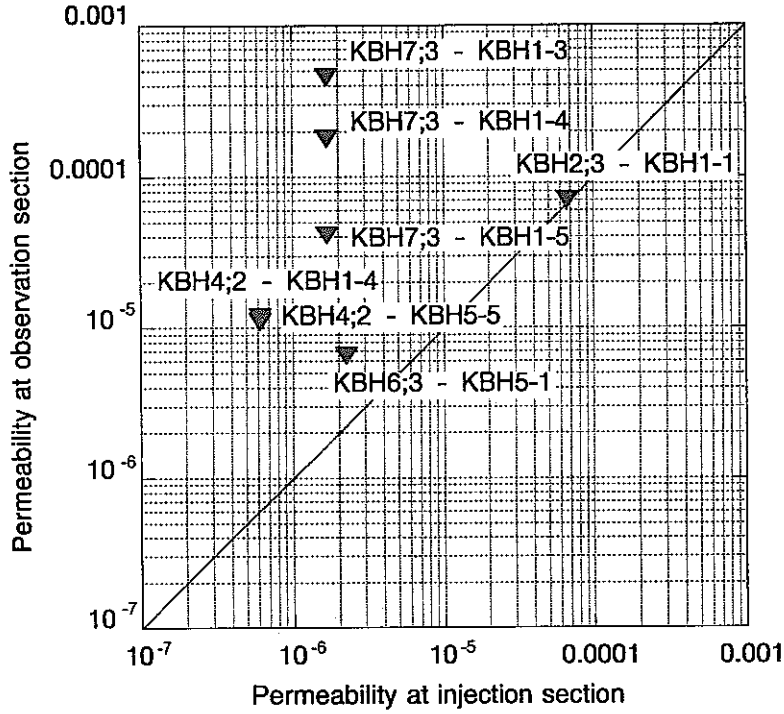

Figure 28 Comparison of the permeability between injection and observation sections

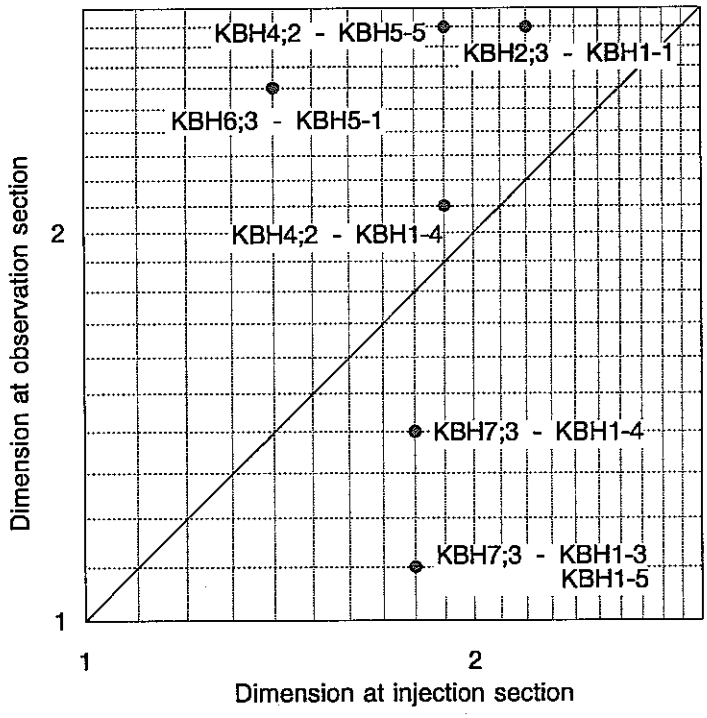

Figure 29 Comparison of the dimension between injection and observation sections

4.4.3 ESTIMATION OF PERMEABILITY TENSOR

Next, these response at the observation wells are analyzed by using the theory proposed by Hsieh, et al[8]. which can obtain the permeability tensor from the interference test.

The unit vector between injection and observation points is $\mathbf{e}$. If the diffusion coefficient (K_f/S_S) tensor, $\mathbf{U}$, exists for the region, the following equation is given;

$$\mathbf{e}_j^T \mathbf{U}^{-1} \mathbf{e}_j = \frac{S_s}{K_d(\mathbf{e}_j)} \tag{36}$$

where j of $\mathbf{e}_j$ is not the components of the vector but the test number of interference tests. The development of this equation is written as

$$e_{j1}^2 U_{11} + e_{j2}^2 U_{22} + e_{j3}^2 U_{33} + 2e_{j1}e_{j2}U_{12} + 2e_{j2}e_{j3}U_{23} + 2e_{j1}e_{j3}U_{13} = \frac{S_S}{K_d(\mathbf{e}_j)} \tag{37}$$

where e_{ji} is the components of the $\mathbf{e}_j$ vector. The right hand side is obtained from the analytical examination mentioned above. There are 6 unknown variables, i.e., U_{11}, U_{12}, U_{13}, U_{22}, U_{23} and U_{33}. Thus, if 6 interference tests having a different direction are carried out, 6 equations would be given by using 6 different vectors, $\mathbf{e}_j$ (j=1,6). When the number of the interference tests is over 6, the method of least squares is applied. After getting the component of $\mathbf{U}$, the principal values of $\mathbf{U}$ are examined whether those values are all positive or not. Since the tensor, $\mathbf{U}$, is the positive definite, all principal values should be positive.

In Kamaishi area, 7 interference tests are carried out as shown in Table 6. By using those data, the permeability tensor is examined. It should be noticed at this stage that the distance between points is 1.6-4.5m. Table 7 shows the principal values of the permeability tensor obtained from the interference tests. Since one of three principal values becomes negative, it seems to be difficult that the permeability tensor of the volume, about a

few meter cubic, is used for calculation. This result would be inferred from the fact that the correlation length is less than 1m. A few meter cubic in this area may have a heterogeneous effect of the permeability. Table 8 indicates the direction of the principal values.

Table 7 Principal values of permeability tensor

Permeability (m/s)		
K1	K2	K3
0.00947132	-0.082434	0.0838627

Table 8 Direction of principal values

	Direction of the principal values		
	X	Y	Z
K1	0.942128	0.0721943	-0.327389
K2	-0.208547	-0.6384	-0.740914
K3	0.262495	-0.766312	0.586398

5. SUMMARY

Results of these experiments indicate that permeability around T-H-M experiment site is very low as a whole but a few high permeable fractures exist. Accordingly, when we will carry out evaluation of result of coupled thermo-hydro-mechanical experiment, it will be important how we will evaluate these fractures. Furthermore, connectivity with these permeable fractures exists at the 3m depth below experiment drift floor. This depth is the same as planned depth of center of heater for T-H-M experiment. This is an interesting result.

6. ACKNOWLEDGMENTS

The authors would like to thank Professors Y.Ohnishi of Kyoto university for his useful advice. The presented work was conducted with Hazama corporation, LTD. The authors also wish to thank them for their work.

REFERENCES

[1] Takeda,S. and Osawa,H.; Current Status and Future Program of In-situ Experiments of Kamaishi Japan, Proceedings of International Symposium on In-situ Experiments at Kamaishi, Nov.11-12, 1993, pp.IV-1-12.

[2] Yamato,A., Masuda,S. and Sakuma,H.; High Level Radioactive Waste Management, Proceedings of the 3rd International Conference, 1992, 1, pp.41-48, American Nuclear Society, Illinois, USA.

[3] PNC ; Kamaishi In-Situ Experiment, PNC Technical Review No.85, PNC TN1340 93-001, 1993, pp.152-162. (in Japanese)

[4] PNC ; Current Status of R&D on Geological Disposal, PNC TN1410 94-094, 1994, pp.222-243. (in Japanese)

[5] Barker,J.A.; A Generalized Radial Flow Model for Hydraulic Tests in Fractured Rock, Water Resources research, 1988, Vol.24, No.10, pp.1796-1804.

[6] Stehfest,H.; Numerical Inversion of Laplace Transforms, Communications of ACM.,1970, Vol.13, pp.47-49.

[7] Karasaki,K.; Well Test Analysis in Fractured Media, Ph.D.Thesis, 1987, Lawrence Berkeley Laboratory, University of California.

[8] Hsieh,P.A. and Neuman,S.P.; Field Determination of the Three-Dimensional Hydraulic Conductivity tensor of Anisotropic Media, 1.Theory, Water Resources research, 1985, Vol.21, No.11, pp.1655-1665.